# Temperature Dependence of the Hypervelocity Impact Response of Polyethylene Plates from $T_g$ to $T_m$

Jacob A. Rogers[a,*], Aniket Mote[a], Sidney Davis[a], Paul Mead[a],
Charles U. Pittman, Jr.[c], Edwin L. Thomas[b], Justin W. Wilkerson[a,b], Thomas E. Lacy, Jr.[a,**]

[a] *J. Mike Walker '66 Department of Mechanical Engineering, Texas A&M University, College Station, Texas, 77843.*
[b] *Department of Material Science and Engineering, Texas A&M University, College Station, Texas, 77843.*
[c] *Department of Chemistry, Mississippi State University, Starkville, Mississippi, 39762.*

**Abstract**

All spacecraft continue to face a growing risk of hypervelocity impact (HVI) by micrometeoroids and orbital debris (MMOD). Concurrently, emerging hypersonic weapons pose acute ballistic threats to military and civilian assets. In both cases, the diminishing effectiveness of legacy armor demands the development of specialized, layered HVI protective structures. Ultra-high molecular weight polyethylene (UHMWPE) and high-density polyethylene (HDPE) stand out as promising intermediate layers due to their high mass-specific energy absorption and tailorability. Yet, their behaviors at HVI-induced strain rates ($>10^6$ $s^{-1}$) remain understudied and poorly understood, particularly near their glass transition ($-116°C$) and melt ($130°C$) temperatures. A recent HVI study revealed that, when impacted at room temperature, UHMWPE targets exhibited bulk fragmentation while similar HDPE samples showed extensive melting and visco-plastic flow, differences attributed to molecular mobility. This follow-on study probes the interplay of initial target temperature ($T_0$), impact velocity ($v_0$), and average entanglements per chain ($N_e$) on polyethylene's (PE's) HVI response. 12.7 mm thick UHMWPE and HDPE plates at $T_0 \approx -120°C$, $20°C$, and $140°C$ were subjected to 2.5 km/s and 6.0 km/s HVIs by 6.35 mm diameter aluminum spheres. PE's HVI response was found to be largely governed by a competition between rates of strain and polymer chain relaxation. Lowering $T_0$ for a fixed $N_e$ constrained chain motion analogously to increasing $N_e$ at a fixed $T_0$. This caused HDPE's HVI response to increasingly align with UHMWPE's at similar $v_0$. The opposite was also observed. Increasing $v_0$ alone made both materials more prone to widespread fracture by raising strain rates beyond rates of chain disentanglement and reorientation. The material exhibiting the most visco-plastic flow without subsequent bulk fragmentation lost less mass, had smaller perforations, and better absorbed energy, suggesting that,

*Corresponding author. J. Mike Walker '66 Department of Mechanical Engineering, Texas A&M University, College Station, Texas, 77843, United States.
*Email Address*: jacob_rogers@tamu.edu
**Corresponding author. J. Mike Walker '66 Department of Mechanical Engineering, Texas A&M University, College Station, Texas, 77843, United States.
*Email Address*: telacyjr@tamu.edu

for a given $T_0$ and $v_0$, there is an optimal $N_e$ value that maximizes PE energy absorption. Increasing $v_0$ or decreasing $T_0$ necessitates a reduction in $N_e$ to sustain the degree of molecular mobility that gives maximum energy absorption. These findings motivate the development of a protective structure composed of PE layers, each optimized for an anticipated average strain rate.

*Keywords:* hypervelocity impact (HVI), two-stage light gas gun (2SLGG), polyethylene (PE), UHMWPE, HDPE, impact energy absorption, thermoplastic, semi-crystalline, entanglement density

---

## 1. Introduction and Motivation

All spacecraft, manned or unmanned, face a significant threat of hypervelocity impacts (HVIs) from micrometeoroids and orbital debris (MMOD), with the danger from micrometeoroids escalating during long interplanetary voyages [1, 2]. Similarly, emerging commercial and military hypersonic vehicles continue to present formidable challenges to legacy thermal and ballistic protection measures [3–5]. With impact velocities exceeding 3 km/s (∼Mach 9), HVIs can severely deform, erode, fracture, fragment, heat, melt, vaporize, and even sublimate materials, often leading to catastrophic system and mission failure, or, more critically, loss of life [6–8]. Numerically modeling the HVI response of materials generally involves a combination of constitutive and failure models and equations of state that are empirical in nature [9]. For this reason, protective structure development and optimization usually involves costly HVI experiments *at room temperature* using sophisticated launch apparatuses, such as two-stage light gas gun (2SLGG) aeroballistic ranges [10]. In many practical applications, materials not only see ultra-high impact velocities but also extreme temperatures. Spacecraft in orbit, for example, can experience temperatures ranging −160°C to 120°C [11], while ambient temperatures on Earth can vary from −80°C to 110°C [12]. Materials on the leading edges of hypersonic vehicles are subjected to temperatures exceeding ∼2,000°C [13]. Hence, characterizing the HVI response of materials at extreme temperatures through methodical laboratory tests is essential for the development and application of next-generation protective structures.

Many spacecraft utilize polymers as window materials or as intermediate layers in MMOD (Whipple) shields [14, 15], while ballistic "bulletproof" vests often incorporate polymer composites for enhanced energy absorption [16]. The effectiveness of polymers and polymer composites in these applications, combined with their customizable properties, has positioned them as top choice materials for innovative space and military protective structures. This interest has spurred numerous investigations into the room temperature HVI response of polycarbonate (PC), polymethyl methacrylate (PMMA), polyethylene (PE) and their composites, and more [17–22]. In these previous studies, targets were typically subjected to normal HVIs by projectiles representing anticipated threats (spacecraft debris, dust, ice, *etc.*). High-rate diagnostics and post-impact target characterization methods were used to unravel HVI-induced target deformation and failure, as well

as identify predominant energy absorbing mechanisms. Ultra-high molecular weight PE (UHMWPE) and high-density PE (HDPE), in particular, have been identified as promising intermediate layers in protective structures due to their high tailorability, low density and cost, and relatively high energy dissipation capabilities [23, 24]. Despite their current and anticipated use in extreme environments, these thermoplastics have not been systematically studied under conditions of both extreme temperature and strain rate. In fact, there have been very few HVI experiments at cryogenic temperatures involving *any* type of material [25–27], and even fewer investigations have been conducted with targets pre-heated well above room temperature [28].

UHMWPE and HDPE are commercially available semi-crystalline polymers of $(–C_2H_4–)_n$ that share similar densities ($\rho_0 \sim 0.95$ g/cc) and physical appearances. They primarily differ in average molecular chain length (*i.e.*, degree of polymerization, $n$) or, equivalently, average molecular weight [29, 30]. The average molecular weight is much higher for UHMWPE ($M_w > 3,000$ kg/mol) than for HDPE ($M_w \sim 100$–500 kg/mol) [31]. The longer chains in UHMWPE lead to fewer chain ends per unit weight and more entanglements per chain ($N_e \sim 3,000$–8,000) compared to HDPE ($N_e \sim 120$–250). UHMWPE can be over 60 times (6,000%) more entangled than HDPE! Entanglements generally boost material toughness and deformation resistance by creating an energy-absorbing network that inhibits chain mobility, uniformly distributes stress, increases elasticity, and reduces crack propagation [32–36]. Yet, UHMWPE's entanglements raise its melt viscosity to around $10^{10}$ Pa·s, roughly $10^7$ times more than HDPE's ($<10^3$ Pa·s), hindering standard high shear processing [37]. The variations in $N_e$ and molecular weight influence molecular packing,[1] resulting in different crystallinity degrees (40–75% in UHMWPE and 70–80% in HDPE) and crystalline structure sizes [30, 35]. Chain branching also affects PE's mechanical behavior. Less branching generally promotes crystallinity and density, making processing challenging [38, 39]. Thus, commercial PEs often have been designed to have some degree of short chain branches to facilitate manufacturing (*e.g.*, $CH_3$ groups adjust molecular conformation to reduce melt viscosity). Although detailed information on chain branching and comonomer content is limited, most commercial PEs are remarkably linear (<3% branching) and pure (additives levels <5% by weight) to avoid impeding powder fusion during molding and to preserve mechanical properties [31]. UHMWPE typically has greater tensile strength, abrasion and crack resistance, and *ballistic* impact strength due to these morphological variations. HDPE, with its higher crystallinity, offers a higher tensile modulus but lower strength and wear resistance [40]. UHMWPE is used in high-wear applications such as medical devices (*e.g.*, knee joint replacements) and bulletproof vests in the form of Spectra® or Dyneema® gel spun fibers [41]. HDPE is commonly found in containers and corrosion-resistant piping. Both exhibit excellent chemical resistance. However, their mechanical and dynamic mechanical property differences at

[1] $N_e$ inhibits the growth of parallel chain folding crystals.

extreme temperatures *and* very high strain rates are less well investigated and understood.

Like many polymers, PE's mechanical properties and dynamic behavior are highly sensitive to strain, strain rate, temperature, and pressure. At room temperature, UHMWPE shows significant strain hardening in tension and compression at strain rates up to $\dot{\varepsilon} \sim 10^3$ s$^{-1}$ for strains under 300% [40, 42]. HDPE, however, demonstrates nearly perfect plastic behavior across similar strains and strain rates [40, 43]. HDPE undergoes significant adiabatic heating and thermal softening at rates above $\dot{\varepsilon} \sim 10^{-2}$ s$^{-1}$ [44]. The effective thermal plastic work conversion factor ($0 < \beta < 1$) quantifies the portion of plastic work converted into heat. HDPE tends to covert nearly all plastic work to heat ($\beta \approx 1$), while UHMWPE converts less than half ($\beta < 0.5$) [30, 44]. The *ballistic* impact resistance and deformation behavior of these PEs are well-documented for impact velocities $\sim 10^2$ m/s and $\dot{\varepsilon} < 10^5$ s$^{-1}$ [30, 36, 45–47]. Generally, higher molecular weight enhances impact strength and resistance to thermal softening/melting and crack propagation promoting tearing brittle fractures [48, 49]. Increased crystallinity does improve yield strength but at the cost of impact performance [30, 50, 51]. At and above room temperature, UHMWPE has slightly better ballistic performance than HDPE [30, 52]. However, these findings cannot be directly extrapolated to HVI-induced strain rates ($\dot{\varepsilon} \sim 10^6$–$10^8$ s$^{-1}$). For PE, the time-temperature superposition principle may be used to relate low-rate material data to that for higher rates. In essence, a one decade increase in $\dot{\varepsilon}$ corresponds to a 10°C drop in temperature for both PEs. Employing this superposition to match temperatures corresponding to HVI-induced strain rates, HDPE still showed significant thermal softening. In contrast, UHMWPE demonstrated only mild softening and continued to exhibit strain hardening [44]. This implies that the variation in thermal softening (adiabatic heating) between the two materials could stem from microstructural factors. These findings are consistent with molecular dynamics (MD) simulations of PE subjected to strain rates over $10^6$ s$^{-1}$, which predicted strain hardening, thermal softening, and a linear relationship between yield stress and logarithm of strain rate [53–55].

Some efforts have been made to understand PE's behavior under HVI conditions. For example, Cha *et al.* [24] conducted HVI tests at approximately 4 km/s using 5.56 mm diameter aluminum projectiles, observing that UHMWPE targets showed superior HVI performance compared to Kevlar used in stuffed Whipple shields (*i.e.*, Whipple shields enhanced with lightweight, energy-absorbing layers filling the space between their often metallic plates). Bowering [56] conducted experiments with 4 mm aluminum spheres impacting UHMWPE, HDPE, and PMMA plates at 2.0–6.5 km/s. UHMWPE appeared to absorb more impact energy. However, these studies were more qualitative in nature and raised further questions about PE's fundamental behavior when subjected to HVIs. More recently, Rogers *et al.* [23] carried out a study comparing 6.35 mm thick UHMWPE ($M_w = 4.7 \times 10^6$ g/mol) and HDPE ($M_w = 1.7 \times 10^5$ g/mol) plates, focusing on their distinct bulk responses to 2.0–6.5 km/s HVIs by 10 mm diameter aluminum spheres. For impacts near

2.0 km/s, the impactor was significantly deformed and eroded but largely remained intact. As velocity increased, the projectile progressively fractured and became more pulverized. Regardless of impact velocity, UHMWPE showed a more quasi-brittle response (extensive fragmentation in the ejecta and debris cloud), likely driven by its highly entangled (constrained) chains. Contrarily, HDPE exhibited substantial bulk-melting and large-scale visco-plastic deformation, due to intense adiabatic heating (Fig. 1). Despite having similar debris cloud geometries and leading-edge velocities, UHMWPE targets lost about 40% more mass than HDPE targets (on average) at the same impact velocities, indicating potentially greater momentum and kinetic energy in the UHMWPE debris clouds. HDPE targets had perforation radii around 20% larger than those in UHMWPE. Initial SEM analysis also revealed that while UHMWPE fracture surfaces were flat and resembled brittle fractures, HDPE surfaces exhibited drawn oriented fibrils, thermal melting/softening, and flow.

This reported bulk behavior and performance of PE at ultra-high strain rates is expected to be highly temperature-dependent. For semi-crystalline polymers, higher temperatures generally lead to increased free volume and chain mobility, faster disentanglement rates, shorter relaxation times, reduced viscosity in noncrystalline regions, and ultimately earlier and more complete melting [35]. Conversely, lowering the temperature has the opposite effect. Such temperature-related phenomena are often characterized with reference to a polymer's glass transition temperature ($T_g$) and melt temperature ($T_m$). For UHMWPE and

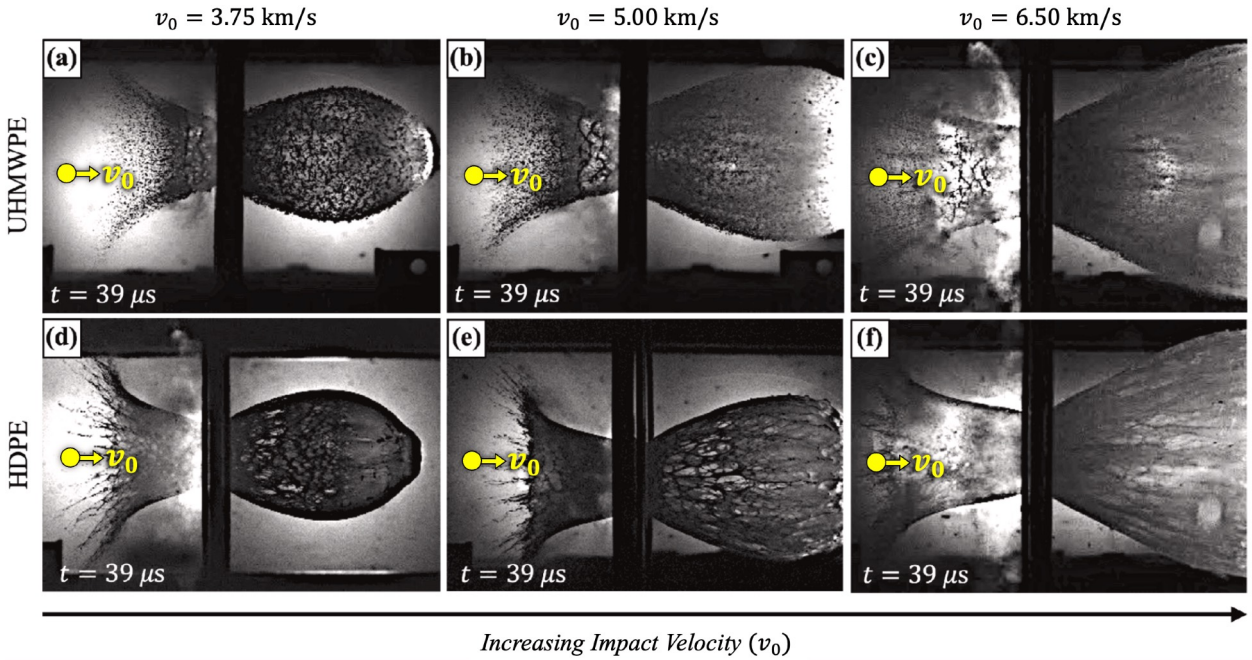


Figure 1: Comparing fully-developed ejecta and debris clouds at different nominal impact velocities in the tested range: (a–c) UHMWPE and (d–f) HDPE. With increasing nominal impact velocity (from left to right), UHMWPE debris fragments become smaller on average, and bulk melting in HDPE becomes more pronounced. Reprinted from Ref. [23].

HDPE, $T_g \approx -120°\text{C}$ and $T_m \approx 130°\text{C}$. Below $T_g$, the free volume is minimal, and polymer chain segment motion is highly constrained. Above $T_g$, a significant increase in free volume enhances chain mobility, transitioning the polymer from a glassy to a rubbery state. However, this transition primarily affects the noncrystalline regions; crystalline regions remain largely intact, interconnected by tie molecules and intercrystalline links that span the amorphous regions. Chain entanglements also contribute to stiffness above $T_g$. Near and above $T_m$, thermal energy overcomes intermolecular forces holding the crystals together, causing them to melt. UHMWPE and HDPE then become viscous liquids, with UHMWPE showing particularly high viscosity due to its dense entanglements. At temperatures much higher than $T_m$, the PEs start to decompose *via* pyrolysis and combustion. This temperature dependent behavior in PE is well characterized for relatively low loading rates ($\dot{\varepsilon} \lesssim 10^2$ s$^{-1}$) [44, 57–59]. However, there have been no comprehensive studies on semi-crystalline PE's HVI ($\dot{\varepsilon} \gtrsim 10^6$ s$^{-1}$) response at temperatures near its glass transition ($T_g$) and melt ($T_m$) temperatures. Therefore, a systematic study probing the interplay of initial target temperature ($T_0$) and impact velocity ($v_0$) on the HVI response of PE could help address fundamental questions about PE's dynamic behavior, as well as shed light on its engineering applications.

The distinct phenomenological responses of UHMWPE and HDPE to HVI, despite their similar density, crystallinity, and chemistry, can likely be attributed to their significant differences in $N_e$. During a HVI, adiabatic shock heating and rapid plastic deformation quickly induce strong gradients in temperature, as well as strain, strain rate, and state of stress, in the target's impacted region that evolve spatially and temporally. PE's poor thermal conductivity intensifies the localized heating. In the HVI tests conducted by Rogers *et al.* [23], HDPE plates exhibited perforation volumes ∼1.4 times larger than those of UHMWPE plates with identical thickness. The average size (pervaded volume) of the UHMWPE chains was roughly 150 times larger than that of the HDPE chains, as estimated by their unperturbed RMS end-to-end distances and molecular weights [60]. These estimates suggest that perhaps 200 times more HDPE chains were involved in deformation, heating, *etc.* compared to UHMWPE chains. For the molecules undergoing rapid deformation, the temperature increase quickly enhances free volume and chain mobility, facilitating chain disentanglement and shortening relaxation times. HVI-induced temperatures can readily exceed the melt temperatures of UHMWPE and HDPE, encouraging bulk melting and flow. However, PE's average molecular weight (chain length) is proportional to the average number of entanglements per chain and inversely proportional to the nominal disentanglement rate. When this disentanglement rate is surpassed by the HVI-induced loading rate, the entangled molecular network becomes virtually frozen, causing internal stresses to rise until chain scission occurs. This phenomenon can be observed macroscopically as brittle failure and bulk fragmentation. One way to probe this hypothesis is to subject UHMWPE and HDPE to extreme strain rates at temperatures from $T_0 < T_g$ to $T_0 > T_m$.

In this study, commercially available 12.7 mm thick UHMWPE ($M_w = 4.7 \times 10^6$ g/mol, $N_e \sim 3,800$, $PDI \sim 10$) and HDPE ($M_w = 1.7 \times 10^5$ g/mol, $N_e \sim 140$, $PDI = 9.6$) plates were subjected to 2.5 km/s and 6.0 km/s HVIs by 6.35 mm diameter 2017-T4 aluminum spheres. The target plates were brought to temperatures below $T_g \approx -120°$C and above $T_m \approx 130°$C using passive cooling and heating methods, respectively. For direct comparison, similar HVI experiments were conducted at room temperature. The PE materials used matched those of Ref. [23], ensuring consistency with previous work. The projectiles were launched using a 2SLGG, and the deformation and failures of the PE were analyzed using high-speed cameras and pre/post-impact characterization. Notably, the HVI response of HDPE shifted from bulk melting to quasi-brittle fragmentation at $v_0 = 2.5$ km/s and $T_0 < T_g$. Conversely, the behavior of UHMWPE started to align with that of HDPE at $T_0 > T_m$. The variations in HVI-induced deformation and failure, as well as HVI performance, were significantly dependent on $T_0$, strongly suggesting that microstructural characteristics, particularly the degree of chain mobility, are responsible for the distinct HVI behaviors of UHMWPE and HDPE observed at room temperature. Numerical simulations of HVIs to PE were used to infer impact conditions.

## 2. Methods

This section provides an overview of the UHMWPE and HDPE materials utilized in this study, as well as target sample preparation and fixturing for HVI experiments. The experimental methodology, with an emphasis on the passive target cooling and heating techniques, is also outlined. A simple conservative metric for comparing debris cloud lethality (*i.e.*, the threat level posed by debris cloud to subsequent structures/assets/personnel) is presented. An overview of the numerical simulation approach is briefly detailed.

### *2.1. Materials and Sample Preparation*

Monolithic plates of UHMWPE and HDPE with dimensions 600 x 600 x 12.7 mm$^3$ were sourced from Mitsubishi Chemical Advanced Materials (TIVAR® 1000) [61] and King Plastic Corporation (King KPC® HDPE) [62], respectively. TIVAR® 1000 (compression molded GUR 4120 powder) has over 97% purity ($\lesssim$3% processing/lubrication additives) and an average molecular weight of $M_w = 4.7 \times 10^6$ g/mol, as calculated from its melt viscosity using the Margolies equation [63, 64]. The King KPC® HDPE plates were also prepared *via* compression molding, without the use of any additives [65]. The as-received PE plates were cut into smaller 102 x 102 x 12.7 mm$^3$ HVI targets using a band saw. For the remainder of this paper, "UHMWPE" exclusively denotes TIVAR® 1000 and "HDPE" refers solely to King KPC® HDPE. Zhang *et al.* [65] characterized the molecular weight distribution of this HDPE using gel permeation chromatography, reporting number average, weight average, and Z-average molecular weights of $M_n = 1.8 \times 10^4$ g/mol, $M_w =$

Table 1: Material characterization data for UHMWPE (TIVAR® 1000) and HDPE (King KPC® HDPE). Molecular weights for UHMWPE and HDPE were sourced from Refs. [63, 64] and [65], respectively. Additional data, including TGA, DSC, and DMA results previously reported in [23] are also included. Key mechanical properties were sourced from Refs. [61, 62].

| Property | UHMWPE | HDPE | % Difference | Standard(s) |
|---|---|---|---|---|
| Number average molecular weight, $M_n$ [g/mol] | ··· | $1.8 \times 10^4$ | ··· | ··· |
| Weight average molecular weight, $M_w$ [g/mol] | $4.7 \times 10^{6\dagger}$ | $1.7 \times 10^5$ | 190% | ··· |
| Z-average molecular weight, $M_z$ [g/mol] | ··· | $1.0 \times 10^6$ | ··· | ··· |
| Polydispersity index, $PDI = M_w/M_n$ | ··· | 9.6 | ··· | ··· |
| Entanglement molecular weight, $M_e$ [g/mol] | ∼1,250‡ | ∼1,250‡ | 0% | ··· |
| Average entanglements per chain, $N_e \sim M_w/M_e$ | ∼3,800 | ∼140 | 190% | ··· |
| Glass transition temperature, $T_g$ [°C] | −116.1 | −116.2 | 0.1% | ASTM E1640-18 |
| Melting temperature, $T_m$ [°C] | 134.1 | 131.1 | 2.3% | ASTM F2625, D3418 |
| Crystallinity, $\chi$ [%] | 52.5 | 70.2 | 28% | ASTM F2625, D3418 |
| Initial decomposition temperature, $IDT$ [°C] | 439.1 | 423.2 | 3.7% | ASTM E2550 |
| Density, $\rho$ [g/cc] | 0.927 | 0.954 | 2.9% | ASTM D792 |
| Yield strength, $\sigma_y$ [MPa] | 40 | 31 | 25% | ASTM D638 |
| Elastic modulus, $E$ [GPa] | 0.55 | 1.8 | 110% | ASTM D638 |
| Thermal conductivity, [W/(K·m)] | 0.4 | 0.5 | 22% | ··· |
| Izod Impact Resistance | no break | 1.1 | ··· | ASTM D256 |
| Shore D Hardness | 66 | 68 | 3% | ASTM D2240 |
| Specific heat capacity, $c_v$ [kJ/(kg·K)] | 1.8 | 2.3 | 24% | ··· |

†This $M_w$ value was determined using the Margolies equation [64]. Hence, $M_n$, $M_z$, and $PDI$ values are not reported for UHMWPE. ‡This $M_e$ value is generally accepted for linear PE in the melt state [67, 68]

$1.7 \times 10^5$ g/mol, and $M_z = 1.0 \times 10^6$ g/mol, respectively. The polydispersity index was $PDI = M_w/M_n = 9.6$. Acquiring comparable chromatographs for UHMWPE is generally challenging due to its high viscosity and limited solubility [31, 66]. Consequently, there is no available data on UHMWPE's PDI, but it is presumed to be akin to other commercial UHMWPEs ($PDI \sim 10$) [66]. Rogers *et al.* [23] previously reported measured $T_g$, $T_m$, density ($\rho_0$), crystallinity ($\chi$), and initial decomposition temperature ($IDT$) values for each PE, which aligned well with supplier and literature values. $T_g \approx -116$°C for both PEs, while $T_m = 134$°C and 131°C for UHMWPE and HDPE, respectively. The density and crystallinity were lower in UHMWPE ($\rho_0 = 0.93$ g/cm$^3$ and $\chi = 52\%$) compared to that of HDPE ($\rho_0 = 0.95$ g/cm$^3$ and $\chi = 70\%$). UHMWPE experienced an onset of thermal degradation at a slightly higher temperature (439°C) compared to HDPE (423°C). This material characterization data is summarized in Table 1.

The semi-crystalline structure of UHMWPE and HDPE complicates precise determination of their entanglement densities and $N_e$ values. A simple approach to estimate $N_e$ in the melt involves dividing the weight average molecular weight by the entanglement molecular weight (*i.e.*, $N_e \sim M_w/M_e$). An accepted $M_e$ value for linear PE in the melt state is $M_e \approx 1,250$ g/mol [67, 68]. Using this $M_e$ value, $N_e \sim 3,800$ and $N_e \sim 140$ monomer for UHMWPE and HDPE, respectively. Hence, UHMWPE's chains are about 30 times more entangled than HDPE's (*cf.* Table 1).[2] These calculations, while not accounting for the full effect of

[2]As crystals form, they drive entanglements to their surfaces, leaving few or no entangled chains within the crystal itself.

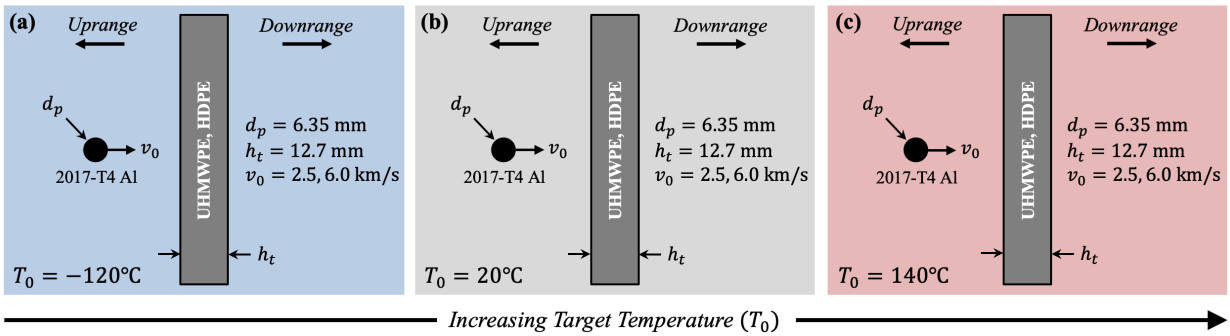


Figure 2: An overview of the HVI testing method. For each PE, 600 x 600 mm$^2$ square plates of thickness $h_t = 12.7$ mm were subjected to $v_0 = 2.5$ and 6.0 km/s impacts at $T_0 \approx$ (a) $-120°$C, (b) 20°C, and (c) 140°C, resulting in twelve total HVI experiments.

molecular weight distribution or crystalline regions, do highlight that the primary distinction between the PEs lies in their $N_e$ values (and molecular weight).

### *2.2. The Impact Experiments*

The HVI experiments were conducted using a 12.7 mm bore 2SLGG, capable of accelerating single projectiles of diameter $d_p = 2.0$–12.7 mm to impact velocities ranging $v_0 = 0.5$–8.0 km/s. Each projectile, encased in a polymer sabot, was launched into an enclosed aeroballistic range (composed of a blast and target tank) under a vacuum pressure of $P \approx 13$ kPa.[3] The sabot separated aerodynamically, enabling the projectile to enter the target tank independently and impact the PE target at normal incidence. The impact velocity of the projectile was measured using laser velocimetry. Further details on the 2SLGG aeroballistic range and testing methodology can be found in Refs. [10, 23, 69]. Experiments were conducted at three distinct initial target temperatures: $T_0 \approx -120°\text{C} < T_g$, $T_0 \approx 20°$C, and $T_0 \approx 140°\text{C} > T_m$. For each $T_0$ value, the PE plates of thickness $h_t = 12.7$ mm were subjected to $v_0 = 2.5$ and 6.0 km/s HVIs by $d_p = 6.35$ mm 2017-T4 aluminum spheres. This procedure led to six HVI experiments per PE type (twelve total), all conducted with a fixed target thickness to projectile diameter ratio of $h_t/d_p = 2$. Hence, for a given PE, the sole variables were $v_0$ and $T_0$, effectively isolating the PE HVI response to particular temperature and impact velocity (strain rate) conditions (Fig. 2). Notably, the chosen $h_t/d_p$ ratio is roughly three times greater than that used in Ref. [23], largely due to a deliberate increase in $h_t$ to enhance the effective thermal mass of the target so as to maintain its $T_0$ before impact.

This process elevates the number of entanglements per volume (entanglement density) in the noncrystalline regions by a factor of $1/(1-\chi)$. Consequently, HDPE concentrates entanglements into its noncrystalline regions by a factor of ∼1.6 times greater compared to UHMWPE.

[3]The tankage assembly was initially evacuated to $P \approx 0.13$ kPa, then backfilled with nitrogen gas until the pressure reached $P \approx 13$ kPa. This procedure aimed to minimize the mixing of $O_2$ with the hot jet of $H_2$ exiting the 2SLGG launch tube [10].

*2.3. Cooling and Heating the Polyethylene Plates*

All four PE targets impacted at $T_0 \approx -120°C$ were first cooled to about $-180°C$ *before* being placed in the target tank (*i.e.*, passive cooling). After sealing the tank, a ten-minute waiting period was necessary to achieve the required vacuum pressure (13 kPa). Benchtop experiments were conducted to characterize the time for the mid-plane of the plate to warm to PE's glass transition temperature ($T_0 = T_g \approx -116°C$). A representative HDPE plate was first cooled in a liquid nitrogen (LN2) bath for about two hours, then exposed to lab air at 20°C. The plate's through-thickness centerline temperature was monitored with thermocouples, revealing a warming time of about eight minutes (Fig 3a). Simple two-dimensional heat transfer calculations indicate that the surface temperature of a representative PE plate, in room temperature air, lags the mid-plane temperature by approximately 5–7°C during the warming period (see Sect. SI.2). When the PE plate was cooled between two 12.7 mm thick steel plates, the warming time exceeded the vacuum time by roughly four minutes. For this reason, a specialized cryogenic fixture was developed to delay the warming time beyond the vacuum period. This fixture enclosed the PE plates on all sides with at least 12.7 mm thick steel, except for 76 mm diameter circular apertures (windows) to be aligned with the projectile impact axis (Figs. 3b and 3c).[4] For all experiments, the projectile perforated the target roughly twice as fast as the time required for shock waves to reflect off the boundaries and return to the impact site (see Section SI.1). Thus, the fixture boundaries had no influence on the perforation event.[5] In lab air tests, the cryogenic fixture extended the target warming times to over fifteen minutes, beyond the required duration for effective HVI testing. Hence, for the cooling experiments, the as-received PE plates cut to 102 x 102 x 12.7 $mm^3$ (Fig. 4a) were placed in the cryogenic target fixture (Fig. 4b), submerged in a LN2 bath for two hours (Fig. 4c), and rapidly transferred to the target tank (Fig. 4e). The tank was immediately sealed and the vacuum pump initiated. A thermocouple, positioned about 30 mm from the target's center, recorded target plate centerline temperatures in the exposed window region (Fig. 3c).[6] When the centerline temperature within the window region reached $T_0 \approx -125°C$, the 2SLGG was fired, accelerating the aluminum spheres to either 2.5 or 6.0 km/s. The impactors reached their targets some ∼300–500 μs later, depending on $v_0$.

For the high-temperature HVI experiments, the same target fixture (Fig. 3b), providing additional thermal mass, was employed. Each of the four 102 x 102 x 12.7 $mm^3$ PE targets intended for impact at $T_0 \approx 140°C$ was initially heated to ∼170°C inside this fixture using an induction burner (Fig. 4d).

[4] An optional feature to cover these windows was available to aid in cooling/heating but was found unnecessary in these HVI experiments.

[5] The boundary conditions set by the steel fixture might have influenced the targets' post-perforation responses to a certain extent. Even so, since all targets shared identical geometries and similar asymmetric boundary conditions during the HVIs, direct comparison is viable/reasonable.

[6] In the benchtop tests, thermocouples measured temperatures at the target centerline both between the steel plates and in the exposed window region. The former showed a lag of ∼10°C.

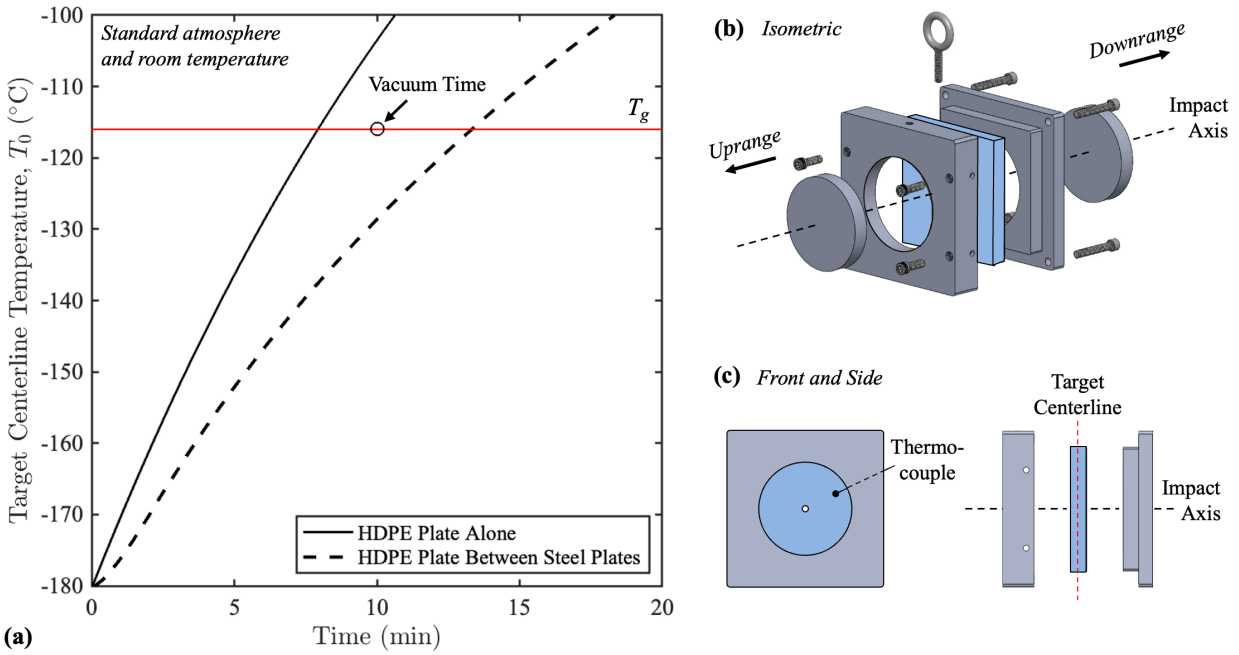


Figure 3: Fixture development for cold-temperature HVI experiments: (a) measurements of through-thickness centerline temperatures of an HDPE plate alone and between steel plates, highlighting extended warming times. Figure (b) displays the cryogenic target fixture in an isometric perspective, with (c) highlighting the thermocouple placement location and target centerline.

Above $T_0 \sim 130$°C, the HDPE targets began to flow/deform. For this reason, each molten plate was placed between two 100 x 100 x 0.050 mm$^3$ square Mylar (polyethylene terephthalate) sheets to retain target thickness and planarity.[7] For both PEs, the assembly remained on the burner until the temperature of both the fixture and the PE plate stabilized. Due to PE's poor thermal conductivity, the entire heating process (from $T_0 \approx 20$°C to $T_0 \approx 170$°C) took approximately thirty minutes, verified by thermocouples and infrared thermometry. After reaching equilibrium, the target assembly was quickly moved to the target tank, which was then sealed, and the vacuum pump activated (Fig. 4e). Similar to the cooling experiments, the centerline temperature of the PE target was continuously monitored in the window region and between the steel plates using thermocouples. The HVI experiment commenced once the target centerline temperature reached $T_0 \approx 145$°C. Following the HVI tests, these targets were quenched in chilled water to arrest post-impact viscous flow. For the four room temperature experiments, no extra thermal mass was needed, so the fixture depicted in Fig. 3b was not employed. Instead, the targets were sandwiched between two 4.8 mm thick steel plates each with a 100 mm diameter circular aperture, similar to the method used in Ref. [23].[8]

[7]Mylar maintains its mechanical strength up to about 150°C and is suitable for use up to 200°C under moderate loads. Hence, the Mylar sheets offered essential support to the molten HDPE target without significantly affecting experimental outcomes, as the projectile interacted with 130 times more HDPE than Mylar (by volume).

[8]This distinct fixture enabled the preparation of low/high temperature experiments concurrently with ongoing room temperature tests.

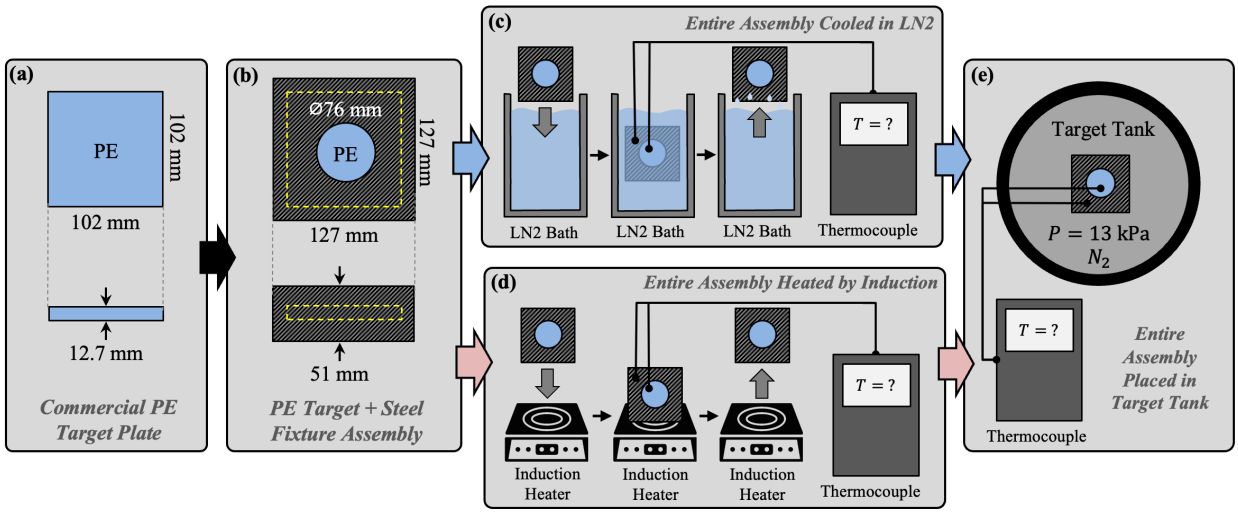


Figure 4: The cooling and heating methodology for the HVI experiments. The (a) as-received PE plates cut to 102 x 102 x 12.7 $mm^3$ were (b) placed in the target fixture, either (c) submerged in a LN2 bath for three hours or (d) placed on an induction burner for sixty minutes, and (e) rapidly transferred to the target tank. Target through-thickness centerline and surface temperatures were monitored using thermocouples.

The room temperature PE target assembly was then placed in the target tank, and once the appropriate vacuum pressure was attained, the HVI experiment was conducted. In all experiments, irrespective of the $T_0$ value, the center of the target fixture aperture coincided with the projectile impact axis, defined by the projectile's velocity vector.

In each experiment, a Shimadzu HPV-X2 high-speed camera, operating at 1 MHz, captured the HVI event *in-situ*, including the projectile's approach, impact, and perforation, as well as the ensuing expansion of the projectile/target ejecta and debris clouds (128 total images per experiment). The camera was oriented orthogonally to the impact axis and configured for shadowgraphic imaging, yielding high-contrast, stop-motion images, consistent with previous HVI experiments involving PE (*cf.* Fig 1) [23]. These images were vital in evaluating how $T_0$ affected target failure and bulk HVI response. Additionally, these images were used in conjunction with motion tracking software to measure the horizontal velocity of the debris cloud's leading edge or tip (*i.e.*, "debris cloud tip velocity") [23]. The PE plates were analyzed pre- and post-HVI to determine target mass loss ($\Delta m_t$). For a number of impacted targets, the perforations were mostly circular in the plane but had irregular/jagged edges. The opening diameter somewhat increased from the front to the back of the target in the through-thickness direction, resulting in a conical perforation surface. For these reasons, the ImageJ software was used to trace the inner-most perimeter of each perforation to measure an effective perforation area ($A_e$). This area was then used to calculate an effective perforation diameter ($d_e = \sqrt{4A_e/\pi}$), representing the diameter of a circle with equivalent area.

### *2.4. Numerical Simulations of HVIs to PE*

The HVI experiments were supplemented with simulations using the Elastic Plastic Impact Computation (EPIC) code, which integrates finite element analysis and smooth particle hydrodynamics for modeling large-scale deformations, fractures, and fragmentation [70]. The simulations calculated impact-induced equivalent plastic strain, strain rate, and temperature distributions for each $T_0$ and $v_0$ combination. The idealized 3D quarter-symmetry PE targets were meshed with tetrahedral finite elements, with element size increasing radially from the impact axis. The projectile mesh size matched that of the target in their contact area. Both projectile and target meshes, totaling $\sim 3 \times 10^6$ elements, were used in all simulations, and a mesh sensitivity analysis confirmed solution convergence. The EPIC code's element-to-particle conversion feature was employed, setting the equivalent plastic strain required for conversion in the target at 30%, a standard value for ductile materials [71]. Projectile and target material behaviors were captured using Mie-Gruneisen equation of state [72], JC constitutive model [73], and JC fracture model [74], with parameters sourced from Ref. [75] and the EPIC materials library. This library notably does not include specific material models for UHMWPE. Consequently, a total of six HVIs into HDPE were simulated to infer HVI-induced conditions in the PE targets during the early stages of target perforation. It is expected that incorporating dedicated UHMWPE models would not substantially change the simulated target response, especially at these early event times. Unfortunately, EPIC's continuum basis significantly limits its ability to represent the microstructural features responsible for the differing HVI responses observed between the two PEs.

### *2.5. A Comparative Metric for Target HVI Performance*

This section briefly introduces a simple debris cloud kinetic energy based metric for comparing the HVI performance of targets subjected to similar impact conditions. A more complete presentation is available in the Supplementary Information, Section SI.3. During a HVI, the projectile's kinetic energy is absorbed through intense deformation, erosion, fracture, fragmentation, heating, melting, vaporization, and sometimes sublimation of both projectile and target. An ejecta cloud usually forms at the impact (front) face of the target, moving "uprange" (*cf.* Figs. 1 and 2) in the opposite direction to the projectile [8, 76]. When perforation occurs, a debris cloud composed largely of molten or solid target material fragments, plus the projectile or its fragments,[9] emerges and expands "downrange" from the target's back side. In non-perforating cratering events, only an ejecta cloud forms. Determining the projectile momentum and kinetic energy absorbed by the target requires resolving the three-dimensional (3D) momenta and kinetic energies of all fragments in the ejecta and debris clouds. This is a challenging task, as differentiating between projectile and target

[9] Vaporized material from the projectile or target may be present in the debris cloud but likely has negligible contribution to the debris cloud's kinetic energy due to its low mass.

fragments in these clouds is nontrivial, even with advanced diagnostics. Additionally, even if a fragment's origin is identified, assumptions about its mass, material state, and 3D geometry would still be required. For ballistic performance studies, the projectile often stays intact and, if perforation occurs, exits the target with residual velocity $v_r$. In such cases, target performance evaluation often focuses on ratios like $v_r/v_0 \sim v_{dc}/v_0$ or a normalized variation of

$$E_p = \frac{1}{2} m_p (v_0^2 - v_r^2), \tag{1}$$

where $E_p$ is typically considered the energy absorbed by the target (see, *e.g.*, [77]). Such an approach is valid since often $\Delta m_t \ll m_p$ and the projectile remains largely intact and undeformed. However, when comparing the *HVI performance* of different target materials, using $v_{dc}/v_0$ or $E_p$ alone is inadequate because (*i*) the projectile rarely stays intact for $v_0 > 2.0$ km/s and (*ii*) a large portion of the target mass is often launched uprange/downrange with significant momentum and kinetic energy. Hence, incorporating target mass loss ($\Delta m_t$) into a comparative metric is advantageous.

When comparing the HVI performance of targets with similar densities and identical geometries impacted by the same projectile, the following assumptions can be made: (*i*) the projectile or its fragments concentrate at the debris cloud tip, (*ii*) the ratio of target material in the ejecta cloud to that in the debris cloud remains similar for all considered impact conditions, and (*iii*) the ratio $v_{dc}/v_0$ between the two materials is assumed to be similar and does not significantly vary with $v_0$ ($v_{dc}/v_0 = 0.45 \pm 0.04$ in this study). Under these assumptions, a simple metric, such as the normalized critical debris cloud kinetic energy[10] can be defined, which accounts for both $\Delta m_t$ and $v_{dc}$:

$$\frac{\tilde{E}_{dc}^j}{E_0^j} = \left( \tilde{\gamma} \frac{\Delta m_t^j}{m_p} + 1 \right) \frac{(v_{dc}^j)^2}{(v_0^j)^2}, \tag{2}$$

where $j$ indexes the experimental observations in set $M$, and $\Delta m_t^j$ is the mass loss and $v_{dc}^j/v_0^j$ is the normalized debris cloud tip velocity for the $j$-th target, respectively. Notably, $0 \leq \tilde{E}_{dc}^j/E_0^j \leq 1$. Here, $m_p$ is assumed to be fixed, and

$$0 \leq \tilde{\gamma} = \min_{1 \leq j \leq M} \left[ \left( \frac{(v_0^j)^2}{(v_{dc}^j)^2} - 1 \right) \frac{m_p}{\Delta m_t^j} \right] \leq 1 \tag{3}$$

is effectively the fraction of $\Delta m_t$ in the debris cloud corresponding to the worst-case scenario among $M$ HVI experiments: the target experiencing maximum mass loss where all projectile kinetic energy is transferred to the debris cloud ($\tilde{E}_{dc}/E_0 = 1$). In this study, the highest HVI-induced normalized target mass loss was $\Delta m_t/m_p \approx 90$, yielding $\tilde{\gamma} \approx 0.04$ for the materials and HVI conditions considered ($v_0 = 2.5$, 6.0 km/s,

[10]The term "critical" is used here to emphasize that all fragments (projectile and target) are assumed to be traveling directly downrange at $v_{dc}$.

$h_t/d_p = 2$). This indicates that for the target experiencing the maximum mass loss, if all $E_0$ were transformed into $E_{dc}$, only $0.04\Delta m_t$ would contribute to the debris cloud's kinetic energy. As an aside, this procedure was used on previous UHMWPE and HDPE HVI data (see Table S2 and Fig. S4) [23], indicating that HDPE marginally outperformed UHMWPE at various impact velocities for fixed target temperature and projectile/target geometry.

## 3. Hypervelocity Impact Experimental Results and Discussion

This section details results for the 2.5 km/s and 6.0 km/s HVIs on the 12.7 mm thick UHMWPE and HDPE plates, whose initial temperatures were set at $T_0 \approx -120$°C, 20°C, and 140°C. *In-situ* high-speed images of the HVIs events, perforation photographs, and performance metric plots are featured. Table 2 summarizes the key experimental results for each combination of PE type, impact velocity ($v_0$), and initial target temperature ($T_0$), including normalized target mass loss ($\Delta m_t/m_p$), target effective perforation diameter ($d_e/d_p$), debris cloud tip velocity ($v_{dc}/v_0$), and critical debris cloud kinetic energy ($\tilde{E}_{dc}/E_0$). Table rows corresponding to $T_0 \approx -120$°C, 20°C, and 140°C are highlighted in blue (cold), white (room temperature), and red (hot), respectively. Impact velocities varied across the experiments, with measurements at $v_0 = 2.49 \pm 0.25$ km/s and $v_0 = 6.17 \pm 0.10$ km/s for each desired $v_0$ value. These fluctuations at a targeted $v_0$ value had little effect on impact loading conditions (*i.e.,* temperature, stress, strain, and strain rate distributions) compared to that resulting from the ∼150% increase from $v_0 \approx 2.5$ km/s to $v_0 \approx 6.0$ km/s (*cf.* Fig. S7). $T_0$ measurements varied within a range of ±2°C and corresponded to PE plate centerline temperatures in the aperture/window region of the fixture (*cf.* Fig. 3c).

In HVI shielding applications, the debris cloud generally poses a more significant threat to subsequent

Table 2: A summary of the temperature-controlled HVI experiments performed in this study (twelve total), including measurements of impact velocity, mass loss, and effective perforation diameter.

| No. | Material | $v_0$ (km/s) | $T_0$ (°C) | $\Delta m_t/m_p$ | $d_e/d_p$ | $v_{dc}/v_0$ | $\tilde{E}_{dc}/E_0$ |
|---|---|---|---|---|---|---|---|
| 1 | UHMWPE | 2.64 | -120 | 1.10 | 1.33 | 0.40 | 0.17 |
| 2 | UHMWPE | 6.10 | -120 | 68.01 | 7.77 | 0.42 | 0.68 |
| 3 | UHMWPE | 2.20 | 20 | 2.39 | 1.14 | 0.47 | 0.24 |
| 4 | UHMWPE | 6.30 | 20 | 13.60 | 3.25 | 0.46 | 0.33 |
| 5 | UHMWPE | 2.69 | 140 | 33.60 | 4.17 | 0.48 | 0.55 |
| 6 | UHMWPE | 6.00 | 140 | 90.32 | 8.87 | 0.46 | 1.00 |
| 7 | HDPE | 2.40 | -120 | 6.42 | 1.60 | 0.40 | 0.20 |
| 8 | HDPE | 6.20 | -120 | 86.83 | 7.83 | 0.41 | 0.75 |
| 9 | HDPE | 2.20 | 20 | 0.73 | 1.42 | 0.44 | 0.20 |
| 10 | HDPE | 6.20 | 20 | 7.98 | 4.65 | 0.45 | 0.27 |
| 11 | HDPE | 2.78 | 140 | 9.86 | 1.50 | 0.37 | 0.19 |
| 12 | HDPE | 6.20 | 140 | 36.10 | 6.33 | 0.35 | 0.30 |

$v_0$, projectile impact velocity; $m_p = 0.372$ g, projectile mass; $d_p = 6.35$ mm, projectile diameter; $T_0$, initial target temperature; $\Delta m_t/m_p$, normalized mass loss; $d_e/d_p$, normalized effective perforation diameter; $v_{dc}/v_0$, normalized debris cloud velocity; $\tilde{E}_{dc}/E_0$, normalized critical debris cloud kinetic energy [Eq. (S14)].

assets, personnel, or infrastructure than the corresponding ejecta cloud. In addition, the debris cloud contains most of the failed projectile/target material. For these reasons, the following discussion prioritizes its formation, expansion, and characteristics. Nevertheless, many conclusions drawn about the debris cloud are also applicable to the ejecta cloud. For each of the twelve HVI experiments, the high-speed camera captured shadowgraphs of the projectile's approach to and impact on the target, as well as the ensuing ejecta and debris clouds. In general, the debris cloud started forming immediately after target perforation. However, the concentration of emerging PE material initially obstructed shadowgraphic light transmission, delaying full visibility of the debris cloud's features until it reached a "fully developed" state. For both PEs, this state was typically achieved at $t \approx 100$ µs regardless of $v_0$, where $t$ denotes the event time relative to projectile impact. High-speed images showing debris cloud development are available in the Supplementary Information, Figs. S5 and S6. Figure 5 displays high-speed images of fully developed debris clouds resulting from $v_0 \approx 2.5$ km/s HVIs into the UHMWPE (left) and HDPE (right) plates, with initial target temperature increasing sequentially from top to bottom: $T_0 \approx -120°$C (Fig. 5a and 5b), $T_0 \approx 20°$C (Fig. 5c and 5d), and $T_0 \approx 140°$C (Fig. 5e and 5f). The UHMWPE and HDPE target locations are highlighted in blue and green, respectively, due to the target assemblies (target inside fixture) being two to four times thicker than the targets themselves. These assemblies were positioned slightly uprange within the camera's field of view (FOV) to better showcase the debris cloud's defining features. Each image displays a scaled projectile icon on the target's uprange side to indicate the direction of impactor motion. In some experiments, the thermocouple wire was visible in the camera's FOV but was far enough from the impact axis to not affect the experiments.

For the $v_0 \approx 2.5$ km/s impacts, both PEs underwent comparable adiabatic shock heating at each $T_0$ due to their similar densities and heat capacities, and each target's local internal energy surpassed the threshold to fully melt the material (see Sect. SI.8). Regardless of $T_0$, the projectile immediately after perforation appeared to be deformed/eroded but largely intact, leading its debris cloud. For the UHMWPE plate, lowering its temperature below $T_g$ resulted in significant target brittleness under the dynamic loading, with a large presence of small particles in the debris cloud (Fig. 5a). This low ($T_0 \approx -120°$C) target temperature further restricted the UHMWPE chains' freedom to move relative to one another while undergoing rapid deformation beyond the constraint already imposed by its extremely entangled molecular network ($N_e \sim 3,800$). Consequently, the increased molecular relaxation times caused stresses to spike, resulting in pronounced brittle fragmentation behavior, even as impact-induced temperatures exceeded $T_m$ (*cf.* Fig. S7). For the same $T_0$, HDPE notably displayed a similar quasi-brittle fragmentation response, with the exception of a minor presence of melted material around and trailing the deformed projectile (Fig. 5b). This molten material, being closest to the projectile during perforation, likely experienced a temperature rise sufficient to overcome

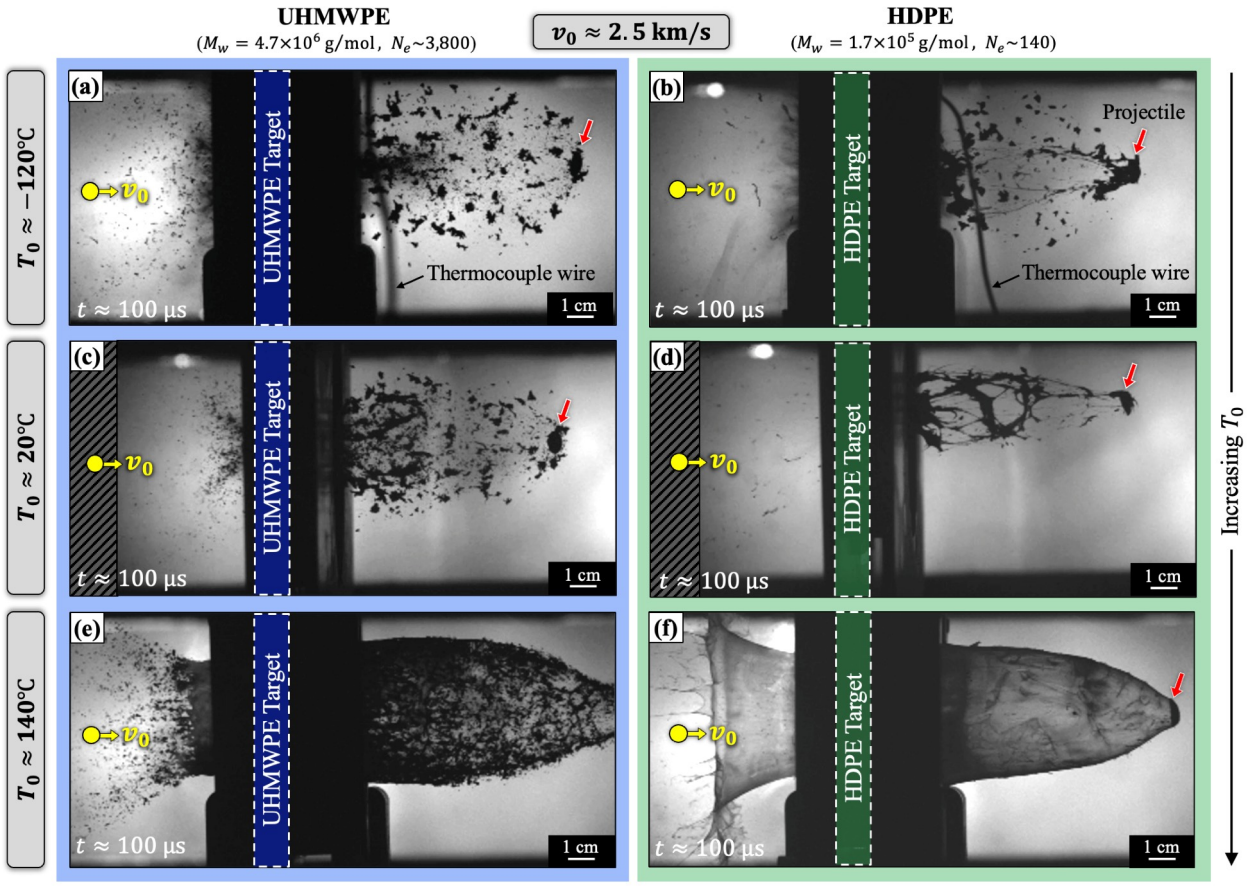


Figure 5: Fully developed HVI debris clouds for UHMWPE and HDPE impacted at $v_0 \approx 2.5$ km/s for temperatures (a, b) $T_0 \approx -120$°C, (c, d) $T_0 \approx 20$°C, and (e, f) $T_0 \approx 140$°C. At $T_0 < T_g$, HDPE shows bulk fragmentation (b) similar to UHMWPE at room temperature (c). At $T_0 > T_m$, UHMWPE's melt response increases (e), aligning its debris cloud geometry closer to that of HDPE (f). Times $t$ are given relative to impact. More debris cloud development is shown in Fig. S5.

the effective chain immobilization caused by its entanglements and depressed $T_0$ value. The low-temperature PEs' fully developed debris cloud envelopes were each traced and then superimposed to underscore their similarities at this $T_0$ value (Fig. 6a). These key observations strongly support the conclusion by Rogers *et al.* [23] that the major differences in the PEs' HVI responses *at room temperature* stemmed from an interplay between the rate of loading and the average rate of molecular disentanglement and reorientation. In essence, lowering $T_0$ for fixed $N_e$ inhibited high-rate chain motion analogously to increasing $N_e$ at fixed $T_0$, making HDPE behave more like UHMWPE when subjected to similar HVIs (more later). At room temperature, UHMWPE and HDPE showed the "bulk fragmentation" and "bulk melting" behavior (Fig. 5c and 5d), respectively, reported in Ref. [23] (*cf.* Fig. 1). This consistency underscores the repeatability of the PEs' HVI responses, even with a nearly threefold increase in $h_t/d_p$.[11] The PEs' dynamic failure behavior differed

[11] As an aside, changing the material manufacturer also does not appear to affect the ultra-high-rate response of each PE at room temperature (*cf.* [56]).

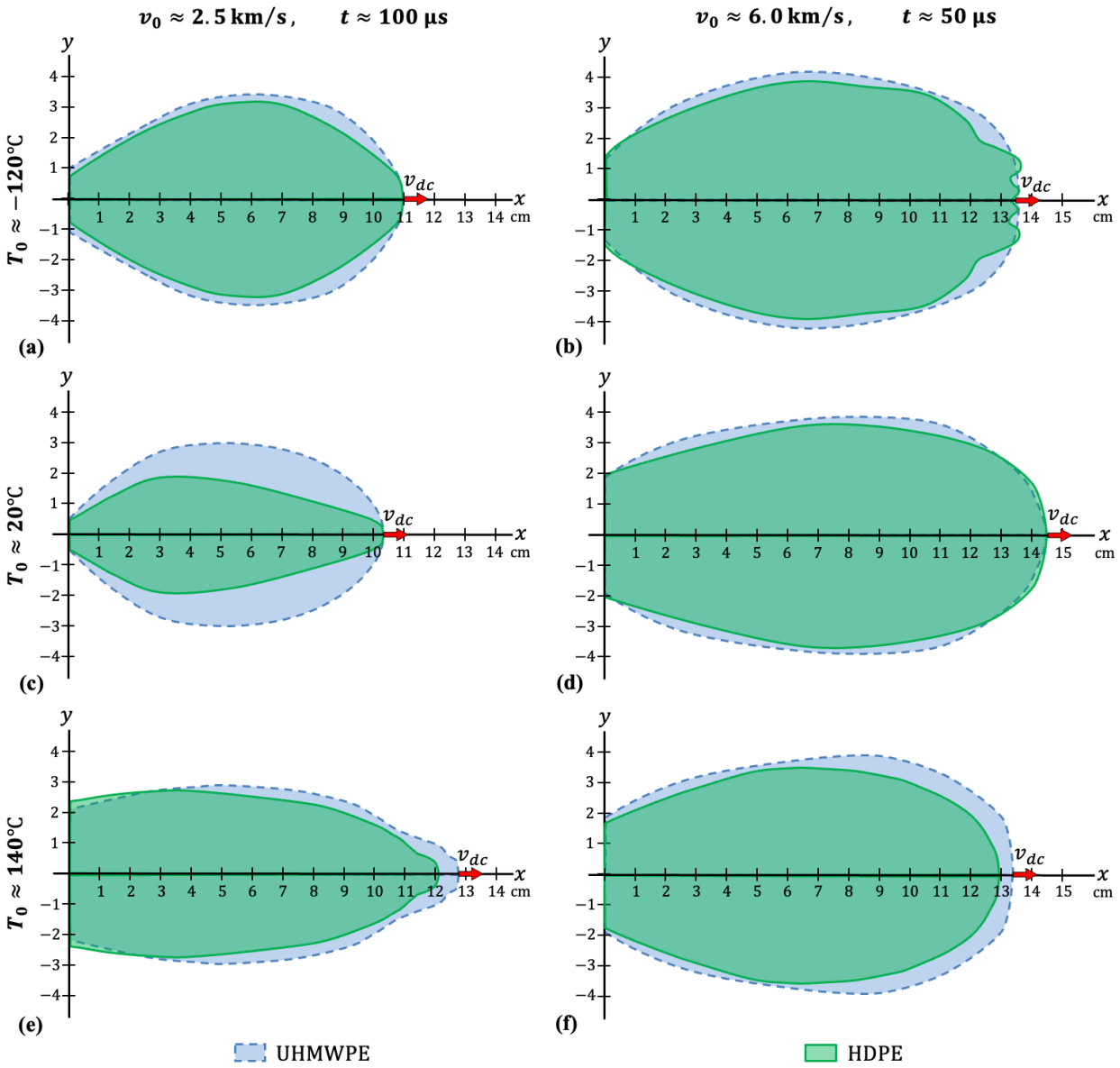


Figure 6: Superimposed HVI debris cloud envelopes for UHMWPE and HDPE at specific temperatures (rows) and impact velocities (columns), with times $t$ given relative to impact. At $T_0 \approx 20°\mathrm{C}$ and $v_0 \approx 2.5$ km/s (c), debris cloud shapes differ significantly, but at $T_0 \approx -120°\mathrm{C}$ and $T_0 \approx 140°\mathrm{C}$, they are similar, indicating comparable failure modes and expansion rates at these transition temperatures. At $v_0 \approx 6.0$ km/s, debris cloud geometries and expansion rates are alike across all $T_0$, showing that temperature sensitivity diminishes as strain rate increases.

the most at this 20°C $T_0$ value, leading to pronounced differences in fully developed debris cloud expansion behavior (Fig. 6c).

For $T_0 > T_m$ and $v_0 \approx 2.5$ km/s, the UHMWPE target's debris cloud was more elongated along the impact axis and denser in appearance due to an increased presence of apparent interconnected material (Fig. 5e). This shift in bulk HVI response at this higher (∼140°C) target temperature is also attributable to the enhanced available molecular motion, which decreases as temperature drops. Increasing $T_0$ above

$T_m$ substantially enhanced free volume, increased rates of disentanglement and reorientation, and shortened relaxation times for the long PE chains. The impact-induced shocks and rapid visco-plastic deformation elevated local temperatures well beyond $T_m$, further amplifying molecular motion (*cf.* Fig. S7). As a result, the molten UHMWPE in the nascent debris cloud flowed readily during early expansion. However, the amorphous polymer network remained extremely entangled and constrained. As the hot expanding material stretched and thinned, it experienced some disentanglement and cooled. The extremely long PE molecules undergoing rapid deformation became increasingly immobile. Instantaneous rates of disentanglement and reorientation dropped and relaxation times spiked. At some critical level of material expansion, the polymer chains could no longer disentangle and/or reorient to relax the rapidly rising stresses. Stress accumulation then gave way to chain scission. Macroscopically, the highly viscous liquid ceased to flow and fractured rather uniformly, producing a dense cloud of UHMWPE fragments. The quasi-brittle HVI responses of room temperature UHMWPE and $T_0 < T_g$ HDPE were also attributed in part to this failure process; however, material fracture occurred prior to such extensive flow, creating noticeably less dense, interconnected, and elongated debris clouds.

A more extreme case of UHMWPE's dynamic failure process explains the characteristic web-like structure seen in the room temperature HDPE target debris cloud (*cf.* Fig. 5d). Initially, this debris cloud resembled a thick, rapidly expanding membrane or "bubble" of continuous molten material. The thickness of this membrane, however, was nonuniform. As expansion continued, its thinner regions experienced disproportionately more biaxial strain, forcing the deforming HDPE chains to disentangle, reorient, and relax in the flow directions faster than those in the thicker regions. Some molecules perhaps even became sufficiently aligned in the strain directions to form strain-induced crystalline domains [78]. Relative chain motion in the more quickly rearranging chains decreased until the thinning bulk material could no longer sustain flow and elongation. Stresses within the local polymer network increased until chain scission occurred. Macroscopically, the membrane material in the thinner regions ruptured and subsequently retracted into the thicker regions as in-plane stresses relaxed. Elongated PE chains returned to more entropically favored conformations, and the average distance between chain ends dropped. Following this rupture process, the thicker regions elongated and formed an expanding network of interconnected molten HDPE fibrils.

Given that both PEs were subjected to similar loading conditions ($v_0 \approx 2.5$ km/s), the difference in their fragmentation/rupture thresholds at a given $T_0$ value is largely due to the drastic difference in their average number of entanglements (*i.e.*, UHMWPE is ~2,600% more entangled that HDPE).[12] Experimental

[12]For the PE plates heated to $T_0 > T_m$, most of the crystalline regions in the semi-crystalline PEs were melted and converted to amorphous arrangements. This suggests that both PEs in the following discussion were both amorphous networks of entangled PE molecules, primarily differing in $M_w$ and $N_e$.

observations support this interpretation. For HDPE heated above its $T_m$, the increased free volume enabled its shorter, less entangled chains to become highly mobile. Adiabatic heating from shocks and rapid visco-plastic deformation further enhanced this molecular mobility to levels sufficient for bulk material flow at extremely high impact loading rates ($\dot{\varepsilon} \sim 10^6$ s$^{-1}$). This shift in microstructural response time facilitated the formation of a membrane-like debris cloud that could sustain remarkable levels of expansion without rupturing (Fig. 5f). Hence, HDPE's debris cloud expansion threshold was significantly extended by a $T_0$-induced increase in chain mobility. In addition, the HVI-induced debris clouds for the UHMWPE and HDPE targets at $T_0 > T_m$ were similar (Fig. 6e). These findings strongly suggest that rising $T_0$ increasingly aligns UHMWPE's HVI behavior with HDPE's. Furthermore, decreasing $T_0$ brings HDPE's response closer to UHMWPE's, provided that $v_0$ is fixed. For both PEs, the degree of debris cloud expansion at which material breakup begins primarily determined the size and shape of debris cloud fragments/fibrils and the level of apparent material connectivity. This threshold is governed by the average rate at which neighboring chains can disentangle and reorient, which depends largely on $T_0$, $v_0$, and $N_e$.

Increasing the impact velocity to $v_0 \approx 6.0$ km/s shortened the perforation event duration by roughly 60%, which in turn raised both the heating and loading rates experienced by the deforming PE material. As a result, local target temperatures well exceeded $T_m$ for both PEs regardless of $T_0$, and strain rates reached $10^7$ s$^{-1}$ (*cf.* Fig. S7). These changes to the temporal and spatial distributions of temperature and strain rate undoubtedly altered the predominant energy absorption mechanisms and dynamic failure behaviors for both PEs. High-speed images of debris clouds resulting from $v_0 \approx 6.0$ km/s HVIs on the roughly $-120$°C, 20°C, and 140°C PE plates are shown in Fig. 7, which is arranged similarly to Fig. 5. At $T_0 \approx -120$°C, UHMWPE's debris cloud consisted of discrete, irregularly shaped fragments of varying size (Fig. 7a), consistent with findings at $v_0 \approx 2.5$ km/s (*cf.* Fig. 5a). The significant fragmentation seen for HDPE at $v_0 \approx 2.5$ km/s and $T_0 < T_g$ was partially reversed at the higher velocity, as the more severe impact-induced heating facilitated more instantaneous chain mobility. Instead, HDPE's debris cloud featured disconnected, elongated fragments (Fig. 7b), shaped by the process that formed its ruptured and unruptured membrane structures at $T_0 \approx 20$°C and $T_0 \approx 140$°C, respectively (*cf.* Figs. 5d and 5f). Yet, when $T_0 \approx -120$°C, impact-induced heating could not raise the target temperature enough to facilitate the same degree of chain elongation, separation, or disentanglement on the time scale of the strain. Hence, the HDPE molecules became effectively frozen within the rapidly stretching fibrils, causing them to fracture prematurely at necking regions during elongation.

At room temperature, the debris clouds for the UHMWPE and HDPE plates impacted at $v_0 \approx 6.0$ km/s exhibited bulk fragmentation (Figs. 7c) and bulk melting (Fig. 7d) responses, respectively, that were virtually indistinguishable from those reported in Ref. [23] (*cf.* Fig. 1). At $T_0 \approx 140$°C, the UHMWPE

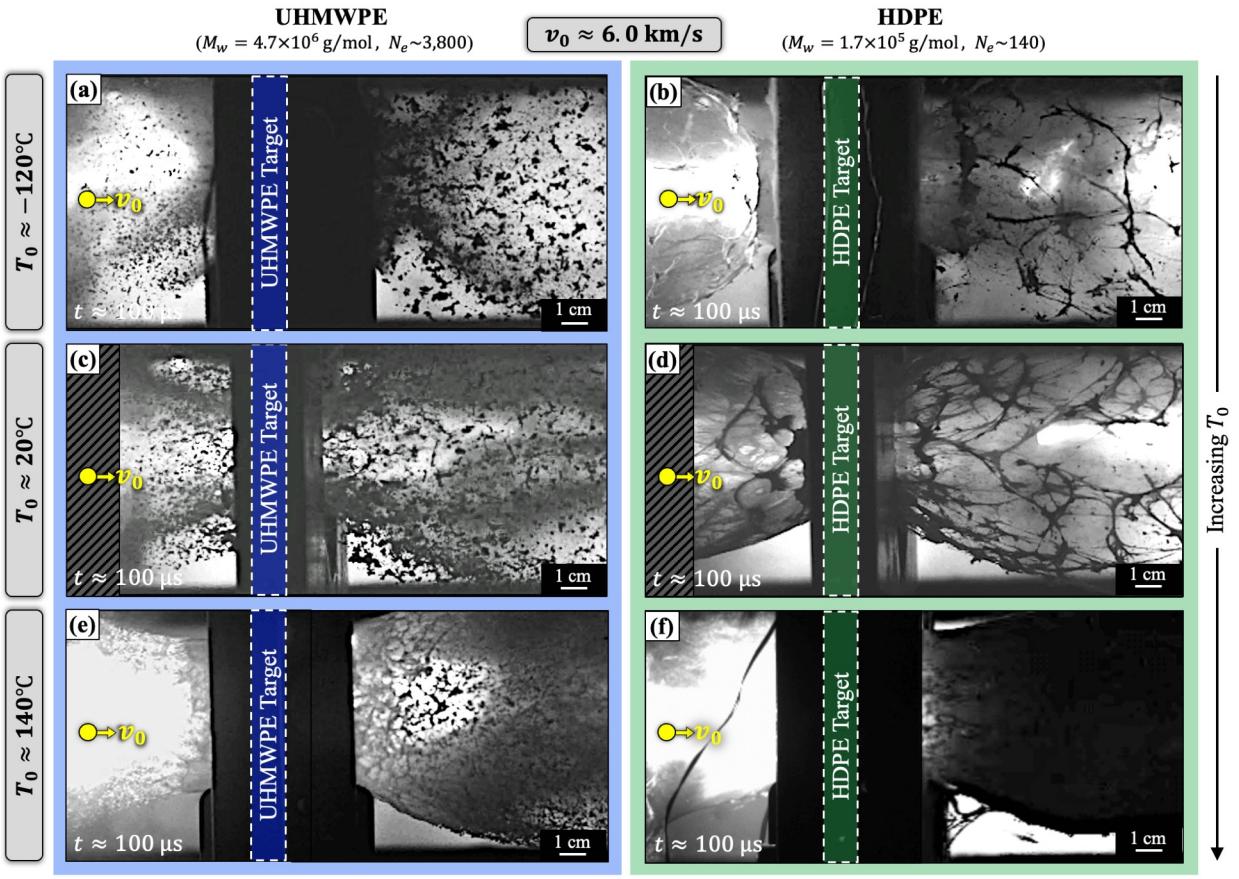


Figure 7: Fully developed HVI debris clouds for UHMWPE and HDPE impacted at $v_0 \approx 6.0$ km/s for temperatures (a, b) $T_0 \approx -120$°C, (c, d) $T_0 \approx 20$°C, and (e, f) $T_0 \approx 140$°C. The fraction of melted material in the UHMWPE debris cloud increases with rising $T_0$ (a, c, e), despite concurrent bulk fragmentation at a given degree of debris cloud expansion (e). Conversely, melting in HDPE decreases below $T_0 < T_g$, although it remains present (b). These findings indicate that the bulk behavior of the PEs is influenced by a competition between temperature, strain rate, and disentanglement rate (chain mobility). Times $t$ are given relative to impact. More debris cloud development is shown in Fig. S6.

debris cloud contained more molten material, as indicated by the presence of a dense web-like structure in its uprange portion, where expansion rates were lowest (Fig. 7e). The HDPE plate impacted under similar conditions displayed a continuous membrane-like debris cloud of molten material that withstood much greater levels of expansion without rupturing (Fig. 7f), similar to observations at $v_0 \approx 2.5$ km/s for the same $T_0$ (*cf.* Fig. 5e). Both PEs' debris clouds densified with rising temperatures, featuring fewer distinct fragments/fibrils and more continuous material. This finding further emphasizes that, at a constant $v_0$, a higher $T_0$ increased the expansion threshold at which debris cloud fragmentation/rupture began due to added chain mobility (*i.e.*, higher rates of disentanglement/reorientation and thus shorter relaxation times). At $v_0 \approx 6.0$ km/s for all $T_0$ values, both PEs showed similar debris cloud geometries and expansion rates, indicating reduced temperature sensitivity at higher loading rates.

The considerable alterations in PE molecular mobility, caused by cooling and heating the targets pre-impact, likewise resulted in significant variations in their deformation and failure features observed post-

impact. For the −120°C UHMWPE plate impacted at $v_0 \approx 2.5$ km/s, the perforation diameter was only marginally larger than that of the impactor (Fig. 8a). Residual out-of-plane deformation was present on both target faces but most prominent on the back side (Fig. 8b). Radial, circumferential, and in-plane target cracks nucleated but were quickly arrested, resulting in a jagged and rough failure surface akin to those seen in similar room temperature samples in Ref. [23]. UHMWPE's quasi-brittle failure was thus mainly localized to the material in contact with and immediately surrounding the projectile during target perforation. The resulting fragments ultimately populated its debris cloud (*cf.* Fig. 5a). The absence of extensive radial or circumferential cracking underscores UHMWPE's strong resistance to crack propagation even when subjected to HVI near its $T_g$. Impact-induced stress waves, however, interacted to focus extreme tensile stresses on an inclined conical plane encircling the impact site. These stresses readily surpassed the material's dynamic strength, causing voids to nucleate. These voids coalesced into a large cone-shaped fracture surface (*i.e.*, "cone crack"), akin to that observed in impacted brittle materials [79]. The spalled material, lacking enough residual momentum and energy for complete ejection, formed a raised circular region on the target's back side (Fig. 8b).

The $T_0 \approx -120$°C HDPE target, impacted at the same $v_0 \approx 2.5$ km/s, showed widespread radial, circumferential, and in-plane cracks (Fig. 8c and 8d). With $T_0 < T_g$, the crystalline regions in the highly crystalline HDPE target could not melt in the impact event's time frame. As HDPE lacked UHMWPE's densely entangled molecular network to facilitate load transfer, stresses concentrated in these regions until they effectively shattered, leading to pronounced brittle failure of the bulk material. The perforation diameter for the HDPE target was almost double that of the projectile. The extreme adiabatic heating during impact softened/melted the material directly around the projectile, resulting in flow patterns on the perforation surface. These features were localized to the inner walls of the opening, as HDPE's poor thermal conductivity inhibited the lateral heating needed to enable any additional material ductility and/or flow. This observation explains the relatively small amount of melted HDPE trailing the deformed projectile in the high-speed images (*cf.* Fig. 5b). There was minimal out-of-plane deformation on either side of the target. Spalled and ejected material from the target's back side, however, left behind a conical indentation concentric with the perforation (Fig. 8d).

The perforation characteristics for the room temperature PE plates impacted at $v_0 \approx 2.5$ were consistent with those observed in Ref. [23]. The effective perforation diameter for the UHMWPE target was slightly smaller than that for the HDPE target (Fig. 8e–8h). The opening in each target was smaller in size than its respective counterpart at the lower $T_0$ value (*cf.* Fig. 8a–8d). For both 20°C PE plates, the impact-induced deformation morphology and failure features were more localized around the perforation. For example, the cone crack and raised circular region were now missing from the UHMWPE target's back side. Yet, its failure

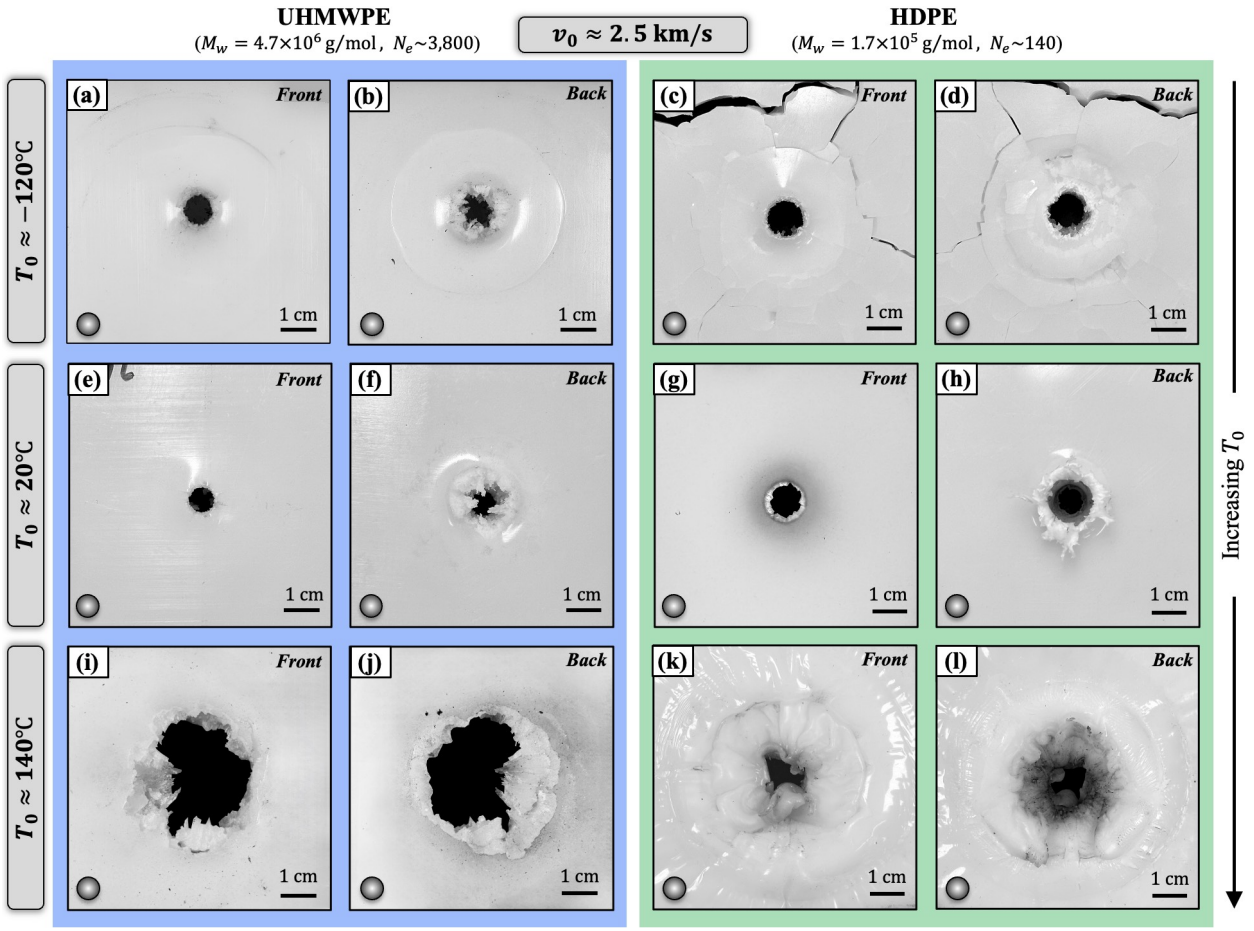


Figure 8: Front and back side images of UHMWPE (left) and HDPE (right) target perforations resulting from HVIs at $v_0 \approx 2.5$ km/s across target temperatures: (a–d) $T_0 \approx -120$°C, (e–h) $T_0 \approx 20$°C, and (i–l) $T_0 \approx 140$°C. For both PEs, perforation diameters ($d_e$) were smallest at room temperature (e–h) and notably increased at $T_0 > T_m$ (c, d, k, l). Residual out-of-plane deformation was also most pronounced for both materials at this $T_0$. UHMWPE resisted crack propagation and flow at each $T_0$, while HDPE exhibited extensive brittle fracture (radial, circumferential, and in-plane cracking) at $T_0 < T_g$ (c, d) and flow at $T_0 > T_m$ (k, l). A projectile is superimposed on each image for scale.

surfaces remained jagged and rough. The comparable HDPE plate showed significant residual out-of-plane deformation on the rear side (Fig. 8h), suggesting extensive impact-induced material softening/melt and flow. Notably, finger-like protrusions on the circumferential rim surrounding the perforation indicated former attachment points of molten drawn HDPE fibrils seen in the high-speed images (*cf.* Fig. 5d).

Heating the targets to $T_0 \approx 140$°C drastically changed the perforations for the same $v_0 \approx 2.5$ km/s. The molten UHMWPE target showed a more jagged, asymmetrical perforation (Fig. 8i and 8j), with its effective diameter increasing by nearly 280% compared to that at room temperature (Fig. 8e and 8f). Virtually no cracks or out-of-plane deformation surrounded the perforation on either target side, and failure surfaces showed minimal signs of melting and flow. Extreme adiabatic heating from impact-induced shocks and rapid plastic deformation raised the target temperature to levels were some material flow was possible, as observed in the early stages of debris cloud expansion (*cf.* Fig. S5i). However, PE's poor thermal conductivity limited

this flow to heated material near and along the impact axis. Target material further (radially) from the impact axis did not experience this temperature rise but still experienced considerable strains, strain rates, and stresses. In these peripheral regions, UHMWPE's molten, but still highly entangled, molecular network lacked the mobility necessary to flow on the time scale of the strain. As the opening expanded radially due to residual momentum and energy in the target material, the highly viscous liquid PE resisted flow, experienced intense stress, and succumbed to melt fracture [80]. Warming the HDPE target dramatically suppressed its viscosity, leading to an increased susceptibility for bulk softening and flow. Consequently, its deformation morphology and failure surfaces differed markedly from those observed at the lower $T_0$ values. For example, the material around the perforation appeared to have been significantly stretched before elastically recovering/retracting post-impact (Fig. 8k). This process produced a target opening with an effective diameter virtually no larger than that seen for the room temperature sample. Significant charring/discoloration present on the failure surface (Fig. 8l) indicated that the impact elevated local target temperatures enough to activate HDPE's thermal degradation, consistent with numerical predictions (*cf.* Fig. S7). Some visco-plastic deformation from stress waves traveling through the target rippled its once flat surfaces. Even so, the elastic recovery of the material in the perforation region minimized residual out-of-plane deformation.

The PE targets experienced significantly more catastrophic failure when impacted at $v_0 \approx 6.0$ km/s, independent of $T_0$. Yet, altering $T_0$ at this velocity did lead to notable variations in the primary deformation and failure mechanisms exhibited by each PE. For instance, the $-120$°C UHMWPE plate showed a perforation roughly eight times larger in diameter than the impactor (Fig. 9a) and five times larger in diameter than that seen for the comparable target impacted at $v_0 \approx 2.5$ km/s (*cf.* Fig. 8a). The morphology of the irregular perforation surface clearly suggested UHMWPE brittle fracture, and residual out-of-plane deformation was virtually nonexistent. A cone-shaped fracture surface, showing signs of extensive charring/discoloration indicative of PE thermal degradation, formed around the perimeter of the opening (Fig. 9b). A large ring-shaped spall fragment, akin to the one not fully detached from the cold target impacted at $v_0 \approx 2.5$ km/s, was ejected following the primary HVI event (*cf.* Fig. S8). At the amplified impact-induced strain rates, UHMWPE's highly entangled microstructure struggled to evenly distributed sharply rising stresses, and the target succumbed to some radial and in-plane cracking. For the same $T_0$, the HDPE plate exhibited an effective perforation diameter similar to that for the $-120$°C UHMWPE target. However, the HDPE plate's target opening had a notably more jagged and non-circular perimeter (Fig. 9c and 9d). The fracture surfaces defining the perforation wall also showed evidence of PE thermal degradation. Extensive radial, circumferential, and in-plane cracking effectively shattered the embrittled HDPE plate during and immediately after impact. Consequently, the plate was kept in the fixture for post-impact perforation imaging, and

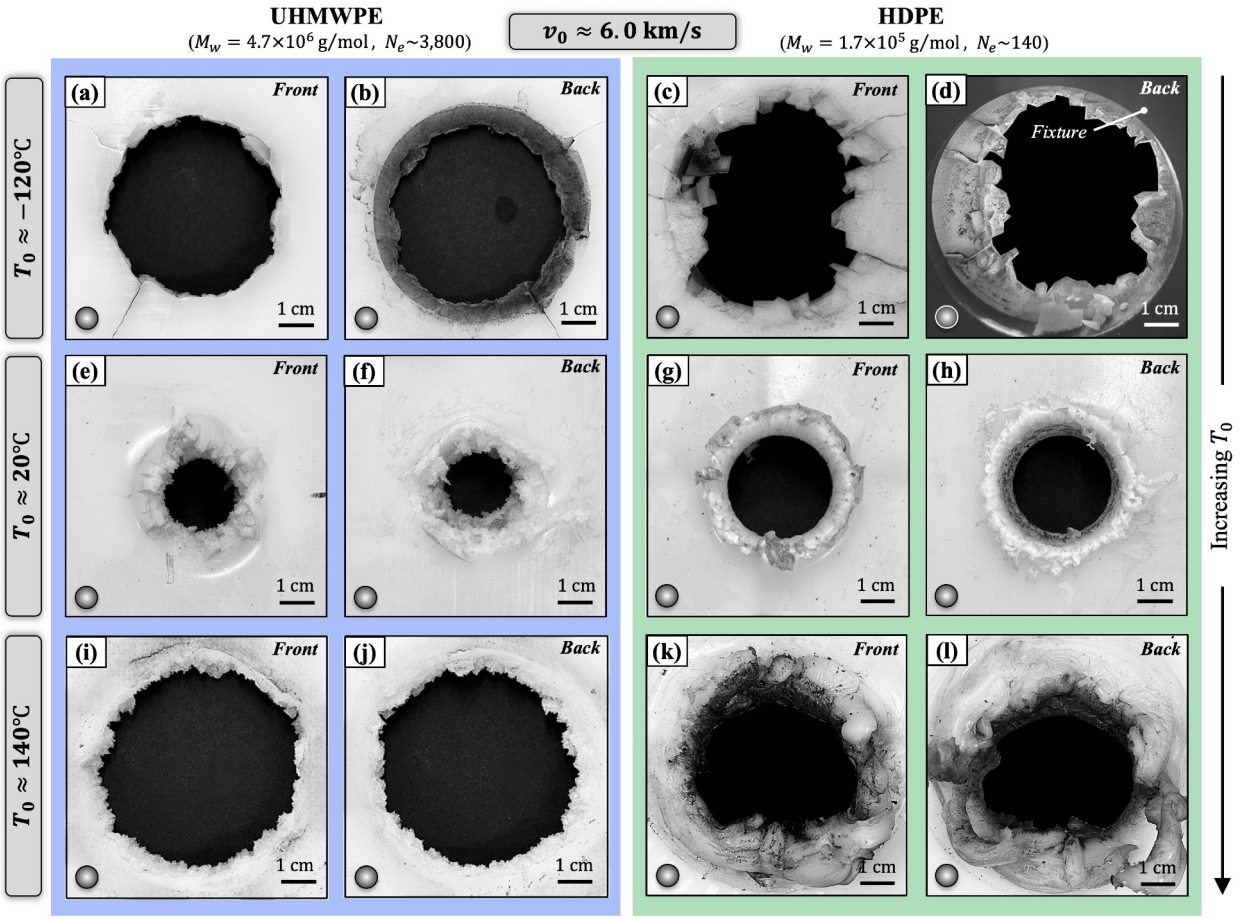


Figure 9: Front and back side images of UHMWPE and HDPE target perforations resulting from HVIs at $v_0 \approx 6.0$ km/s across target temperatures: (a–d) $T_0 \approx -120$°C, (e–h) $T_0 \approx 20$°C, and (i–l) $T_0 \approx 140$°C. At $T_0 \approx -120$°C, UHMWPE still resisted crack propagation, while HDPE exhibited bulk brittle fracture. For the sample in (a, b), a cone fracture surface formed on the exit side, and a large annular fragment was later ejected (Fig. S8). The HDPE sample in (c, d) completely shattered and was thus photographed before removal from the fixture to prevent it from disassembling (Fig. S9). Extensive material flow, as well as charring (thermal degradation), were evident for the HDPE target at $T_0 \approx 140$°C (k, l). Out-of-plane deformation was most pronounced for both PEs at room temperature. A projectile is superimposed on each image for scale.

the fragments were collected and imaged once removed from the fixture (*cf.* Fig. S9).

The predominant deformation and failure features observed for each room temperature PE target impacted at $v_0 \approx 2.5$ km/s did not appear to change when $v_0$ was increased to 6.0 km/s. In addition, they continued to align with those from similar HVI experiments presented in [23]. However, the faster perforation event at $T_0 \approx 20$°C resulted in much more severe out-of-plane deformation for both PE targets, especially on their front faces (Figs. 9e–9h). The ~150% increase in $v_0$ resulted in a 200% and 236% increase in effective perforation diameter for the $T_0 \approx 20$°C UHMWPE and HDPE targets, respectively. The fracture surfaces originally seen in the UHMWPE sample impacted at $v_0 \approx 2.5$ km/s were even more apparent at the higher velocity. The opening's in-plane perimeter was highly irregular due to short radial cracks, and stunted in-plane cracks caused the surrounding material to fan out perpendicularly. Together, these cracks

formed a perforation wall with a distinctive peak-and-valley morphology (Fig. 9e and 9f). Conversely, the HDPE target impacted at $v_0 \approx 6.0$ km/s displayed smooth perforation surfaces with clear signs of material softening, melting, and flow at 20°C (Fig. 9g and 9h). The finger-like protrusions that were noticeable on the back surface of the room temperature target impacted at $v_0 \approx 2.5$ km/s became more defined and were also present on the impact side. Material thermal degradation was evident along the inner surface(s) of the opening for both PEs. On its front side, the HDPE target also showed signs of thermal degradation along the rim of out-of-plane deformation that surrounded the perforation (Fig. 9g).

Elevating the PE targets' temperature to $T_0 \approx 140$°C again significantly altered their perforation morphologies when impacted at $v_0 \approx 6.0$ km/s. Despite $T_0$ exceeding $T_m$, the UHWMPE plate still exhibited jagged, brittle-like fracture surfaces that lined the perimeter of the perforation (Fig. 9i and 9j), which was 170% larger in effective diameter than that of the 20°C target impacted at the same $v_0$ (Fig. 9e and 9f). Any signs of the molten, flowing material visible in the high-speed images (*cf.* Fig. S6i) were erased/removed as the perforation expanded due to residual momentum and energy in the surrounding target material (residual hole enlargment). At some degree of UHMWPE hole enlargement, the cooler, yet molten, encircling material ceased flowing and started to experience melt fracture, mirroring the behavior seen in the 140°C target impacted at 2.5 km/s (*cf.* Fig. 8i and 8j). This was not the case for the 140°C HDPE target impacted at 6.0 km/s. Instead, its perforation was encircled by material that had undergone extensive flow, elongation/stretching, fracture/puncture, and elastic recovery (Fig. 9k and 9l). This HDPE deformation and failure resulted in an asymmetrical perforation roughly 30% smaller than that seen in the 140°C UHMWPE plate impacted at the same $v_0$ (*cf.* Fig. 9i). The HDPE perforation was encircled by finger-like protrusions, which were fewer in number but larger in diameter than those seen on comparable targets impacted at lower $T_0$. Failed target surfaces for both PEs appeared significantly charred, indicating some material pyrolysis and combustion had occurred.

The perforated plates were also inspected *quantitatively* to better characterize and understand the differences in their HVI-induced responses. The mass of each PE target was measured before and after impact to determine its normalized mass loss ($\Delta m_t/m_p$). For both PEs across all $T_0$, these values increased with impact velocity ($\Delta m_t/m_p \propto v_0$). At $v_0 \approx 2.5$ km/s, the $\Delta m_t/m_p$ values for UHMWPE showed a monotonic increase with $T_0$, rising nearly thirtyfold from −120°C to 140°C (Fig. 10a). This trend, however, did not hold for $v_0 \approx 6.0$ km/s. Instead, the 20°C UHMWPE target lost ∼80–85% less mass than the −120°C and 140°C plates. This transition underscores the intricate interplay of $T_0$, $v_0$, and molecular mobility on dynamic material behavior/failure. In essence, lowering $T_0$ does make PE more brittle but simultaneously decreases the fraction of material undergoing visco-plastic flow during perforation. UHMWPE's flow, elongation, cooling, and ultimate fracture *is* what primarily drives its fragmentation. At $v_0 \approx 2.5$ km/s, decreasing

$T_0$ suppressed UHMWPE flow without inducing additional fracture/fragmentation, enabling a consistent reduction in $\Delta m_t/m_p$. Conversely, the 6.0 km/s impact into the −120°C UHMWPE target *did* cause more material to fracture, and the resulting fragments (including the spall fragment) together had sixty times more mass than that ejected from the −120°C target impacted at the lower velocity (*cf.* Figs. 9a and 9b). At $T_0 \approx 140$°C, the UHMWPE target's mass loss was maximized for both $v_0$, as increased bulk material flow gave way to extensive melt fracture (*cf.* Figs. 9i and 9j). These results show that the degree to which a PE target will fracture/fragment (*i.e.*, lose mass) as $T_0$ and/or $v_0$ vary is largely governed by the proportion of its material that can simultaneously resist flow and retain toughness. Hence, at a given combination of $v_0$ and $T_0$, the PE plate exhibiting the highest level of combined bulk flow and quasi-brittle fragmentation loses the greatest mass (*e.g.*, the UHMWPE plates at $T_0 \approx 140$°C).

This finding also aligns with the HVI response of the HDPE targets. At $T_0 \approx -120$°C, both HDPE targets experienced widespread brittle fracture (cracking), leading to 80–100% more mass loss than its room temperature samples (*cf.* Figs. 8c, 8d, 9c, 9d). The 140°C HDPE targets likewise experienced more mass loss but due to extensive visco-plastic flow, elongation, and moderate fracture (*cf.* Figs. 8k, 8l, 9k, 9l). These $T_0$-induced transitions in HDPE's HVI response resulted in trough-shaped $\Delta m_t/m_p$ *vs.* $T_0$ trends for both $v_0$ (Fig. 10a). All 20°C and 140°C HDPE targets, experiencing primarily thermal softening/melting and flow, consistently lost less mass than the comparable UHMWPE targets, consistent with findings from Ref. [23]. However, this relationship was reversed at $T_0 \approx -120$°C due to HDPE embrittling more than UHMWPE. Interestingly, the highest target mass loss value for each PE was achieved at opposite extremes of the $T_0$ range, with both losing around ninety times the projectile's mass. Comparable data from Ref. [23] ($h_t/d_p = 0.64$, $m_p = 1.41$ g) is also displayed on the plot for comparison.

Perforations were also compared across experiments using their normalized effective diameter ratios ($d_e/d_p$). In general, $d_e/d_p$ increased with impact velocity. For each $v_0$, the perforations in the −120°C and 20°C HDPE targets were larger than those in the similar UHMWPE targets (Fig. 10b), a trend consistent with findings reported in Ref. [23]. However, at $T_0 \approx 140$°C, the UHMWPE targets had larger $d_e/d_p$ values, as they underwent substantial post-impact residual hole enlargement *via* melt fracture (*cf.* Figs. 8i and 9i). Such hole enlargement was suppressed in the hot HDPE melted plates due to the material elastic recovery/retraction that occurred post-perforation (*cf.* Figs. 8k and 9k). The HDPE targets impacted at 2.5 km/s showed no significant change in $d_e/d_p$ with varying $T_0$, though there were some variations at $v_0 \approx 6.0$ km/s. At room temperature, the HDPE targets showed larger $d_e/d_p$ values but less mass loss compared to the UHMWPE targets because of HDPE's capacity for large-scale plastic deformation, as opposed to UHMWPE's tendency to fragment (*cf.* Fig. 10a). At $T_0 \approx -120$°C and 140°C, larger perforation diameters were associated with greater mass loss values for both PEs regardless of $v_0$, a change attributed

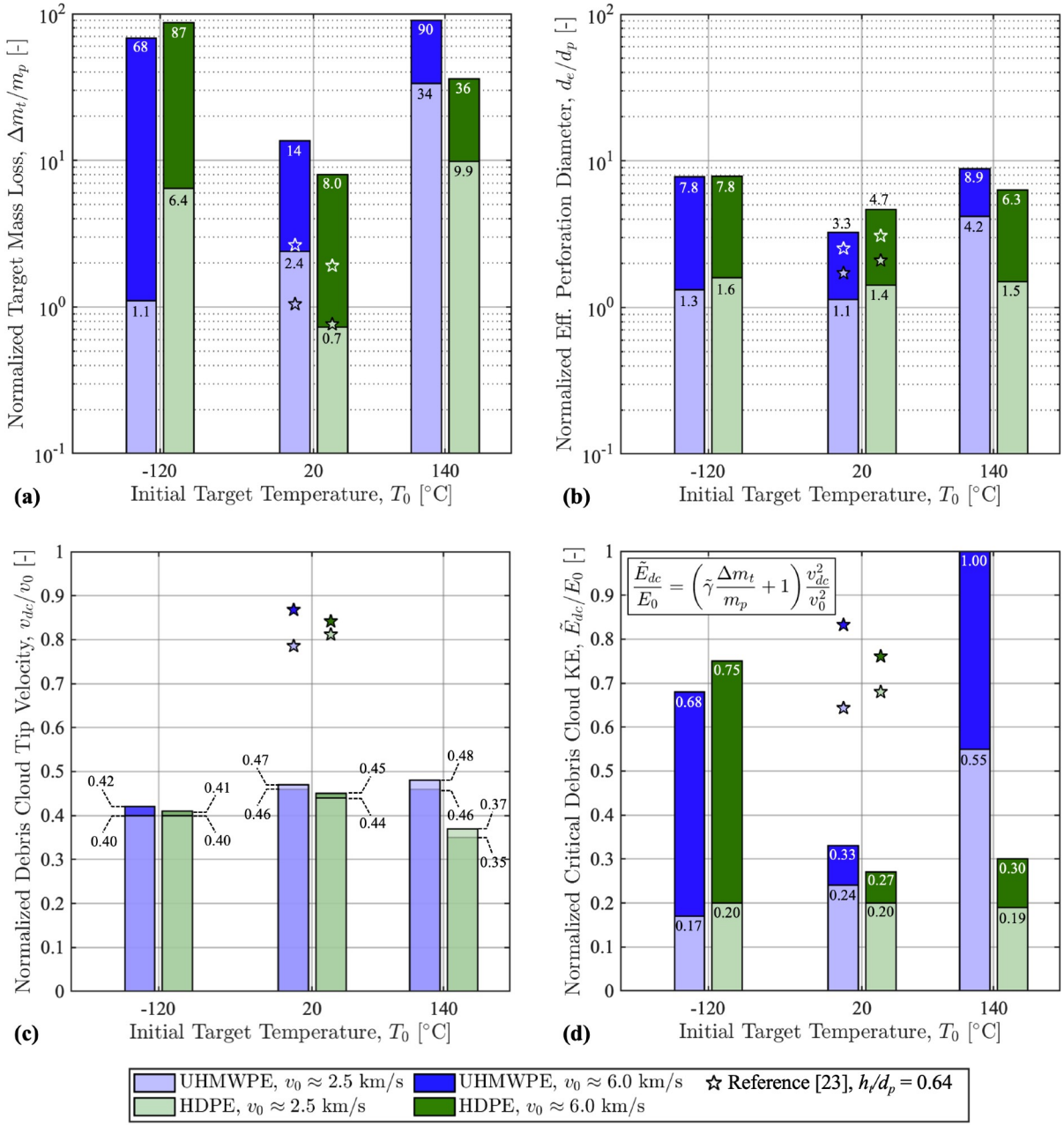


Figure 10: Response of UHMWPE and HDPE plates to HVIs at $v_0 \approx 2.5$ km/s and 6.0 km/s and $T_0 \approx -120$°C, 20°C, and 140°C: normalized (a) mass loss, $\Delta m_t/m_p$; (b) effective perforation diameter, $d_e/d_p$; (c) debris cloud tip velocity, $v_{dc}/v_0$; and (d) critical debris cloud KE, $\tilde{E}_{dc}/E_0$; all *vs.* $T_0$. For a given PE, $\Delta m_t/m_p$ was greater at the transition temperatures, expect for UHMWPE at $v_0 \approx 2.5$ km/s and $T_0 \approx -120$°C (a). $d_e/d_p$ (b) also increased at $T_0 \approx -120$°C and 140°C. $v_{dc}/v_0$ nominally increased with $T_0$, expect for the case of HDPE at $T_0 \approx 140$°C. Considering $\Delta m_t$ indicates significant variation in KE absorption with $T_0$ for both PEs (d). Data reported in Ref. [23] for $h_t/d_p = 0.64$ is included for reference.

to HDPE's distinct deformation behaviors and failure mechanisms at the extreme temperatures.

Analyzing the high-speed *in-situ* images of each HVI event offered insight into the PE targets' relative degrees of energy absorption. For each experiment, the debris cloud's downrange-most tip was tracked over

time (along the impact axis) to calculate its average velocity ($v_{dc}$).[13] This velocity was then normalized by the corresponding $v_0$ for comparison with the other experiments. The $v_{dc}/v_0$ values for the UHMWPE targets impacted at 2.5 km/s increased by 15–20% from $T_0 \approx -120$°C to $T_0 \approx 140$°C ($v_{dc}/v_0 \propto T_0$; Fig. 10c). A similar increase was seen between the −120°C and 140°C UHMWPE targets impact at 6.0 km/s; however, there was virtually no change in $v_{dc}/v_0$ from $T_0 \approx 20$°C to $T_0 \approx 140$°C. The normalized tip velocities similarly increased for the −120°C and 20°C HDPE targets. These $v_{dc}/v_0 \propto T_0$ trends align with expectations, as increases in temperature typically reduce material viscosity, hardness, and strength due to enhanced chain mobility. Notably, UHMWPE's densely entangled microstructure fought activation of any new/additional predominant energy dissipation mechanisms as $T_0$ and $v_0$ varied. For all $T_0$, the $v_{dc}/v_0$ values for the UHMWPE plates were the same as or higher than those for the HDPE targets, a finding that suggests HDPE absorbed more projectile energy ($E_p \propto 1 - (v_{dc}/v_0)^2$, excluding $\Delta m_t$ contribution; *cf.* Eq. 1). The normalized tip velocities for the 140°C HDPE plates were notably the lowest among all targets, regardless of $v_0$ or $T_0$. In particular, they were about 25% lower than those for the UHMWPE targets heated to the same temperature (Fig. 10c). This reversal in HDPE's trend [*i.e.*, $v_{dc}/v_0 \propto T_0 \rightarrow v_{dc}/v_0 \propto 1/T_0$] suggests that (*i*) there is a shift in its predominant energy dissipation/failure mechanisms, (*ii*) these mechanisms are being engaged for a longer duration of time, or (*iii*) more mechanisms are being activated simultaneously (more later). Comparable debris cloud tip velocity data for the HVI samples in Ref. [23] are plotted in Fig. 10c for comparison.

Using the normalized critical debris cloud kinetic energy ratio [$\tilde{E}_{dc}/E_0$, *cf.* Eq. (2)] to account for the combined effect of target mass loss and debris cloud tip velocity may provide better insight into each PE target's relative energy absorption ($E_p \propto 1 - \tilde{E}_{dc}/E_0$) and thus HVI performance. Since $v_{dc}/v_0$ saw only moderate variation with $v_0$ and $T_0$ for both PEs, the $\Delta m_t/m_p$ value for a given target somewhat dominated the magnitude of its $\tilde{E}_{dc}/E_0$ ratio. Hence, the PEs' trends in $\tilde{E}_{dc}/E_0$ with $T_0$ and $v_0$ tended to align with those seen in Fig. 10a. One exception is the HDPE targets impacted at 2.5 km/s, which showed no change in $\tilde{E}_{dc}/E_0$ with initial target temperature. In fact, except at $T_0 \approx -120$°C, the HDPE targets showed less sensitivity to changes in impact velocity (average strain rate) and temperature (molecular mobility) compared to UHMWPE targets. This distinction is attributable to their vastly different entanglement densities. For each $v_0$, the ∼20°C and ∼140°C HDPE targets, which did not experience brittle fracture/fragmentation, appeared to better absorb projectile kinetic energy compared to the similar UHMWPE targets. Put differently, the UHMWPE debris clouds possessed higher total kinetic energy, a finding consistent with previous work [23]. At $T_0 \approx -120$°C, the tougher UHMWPE targets better resisted crack propagation, fragmentation, and

[13] The variations in the $v_{dc}$ measurements, caused by the camera's pixel resolution, were approximately ±0.05 km/s.

mass loss, leading to marginally lower $\tilde{E}_{dc}/E_0$ values compared to those for the comparable HDPE plates. At $v_0 \approx 6.0$ km/s, raising $T_0$ from about $-120$°C to room temperature enhanced the performance of both PEs, primarily because increased molecular mobility facilitated strain delocalization and more visco-plastic deformation/flow. Increasing $T_0$ further to roughly 140°C resulted in virtually no change to HDPE's performance at a given $v_0$ due to additional thermal softening/melting supporting progressively more material flow. Conversely, the ∼140°C UHMWPE target experienced a sharp drop in performance for both $v_0$. *These results strongly suggest that, for a PE target impacted at a given $v_0$, there exists an optimal $T_0$ value or, alternatively, degree of molecular mobility, that maximizes its energy absorption* ($E_p$). The debris cloud tip velocity measurements independently support this conclusion [*i.e.*, $E_p \propto 1 - (v_{dc}/v_0)^2$; *cf.* Fig. 10c].

The pre-impact, *in-situ*, and post-impact findings together affirm that differences in deformation behavior, failure modes, and relative energy absorption between UHMWPE and HDPE can essentially be attributed to molecular mobility. At a constant $N_e$ value, raising the temperature of a given PE target increases its free volume, promotes chain disentanglement and reorientation, and reduces relaxation times. Conversely, increasing $N_e$ at constant $T_0$ has the opposite effect. When subjected to HVI, a PE target with less constrained chains will experience increased large-scale thermal softening/melting and flow. Under identical impact conditions, imposed constraints on the target's microstructure, either by reduced $T_0$ or elevated $N_e$, will induce more pronounced quasi-brittle fragmentation. Increasing $v_0$ alone can effectively embrittle a target by raising the average strain rate [$\dot{\bar{\varepsilon}} = f(v_0, h_t, d_p, \dots)$] beyond the rates of disentanglement and reorientation. The target that exhibits the most visco-plastic flow without bulk fragmentation will generally lose less mass, have smaller perforations, and better absorb energy. These observations suggest there is a critical average number of entanglements,

$$N_e^* = f(T_0, v_0, h_t, d_p, \dots) = f(T_0, \dot{\bar{\varepsilon}} \dots), \tag{4}$$

that, for fixed $v_0$, $T_0$, and projectile-target combination, characterizes a PE target's transition in HVI response from extensive quasi-brittle fragmentation to bulk thermal softening/melting and flow. Hence, the proximity of a target's $N_e$ value to $N_e^*$ is a strong indicator of its ability to absorb energy. In general, the energy absorbed by a target subjected to HVI can be expressed as

$$E_p = \int_0^{\tau} \dot{E}_p(t)\, dt, \tag{5}$$

where $\tau$ represents the time (relative to impact) at which the projectile (or its fragments) and the target cease to interact, $t$ is the event time, and $\dot{E}_p(t)$ is the target's instantaneous energy dissipation rate. The

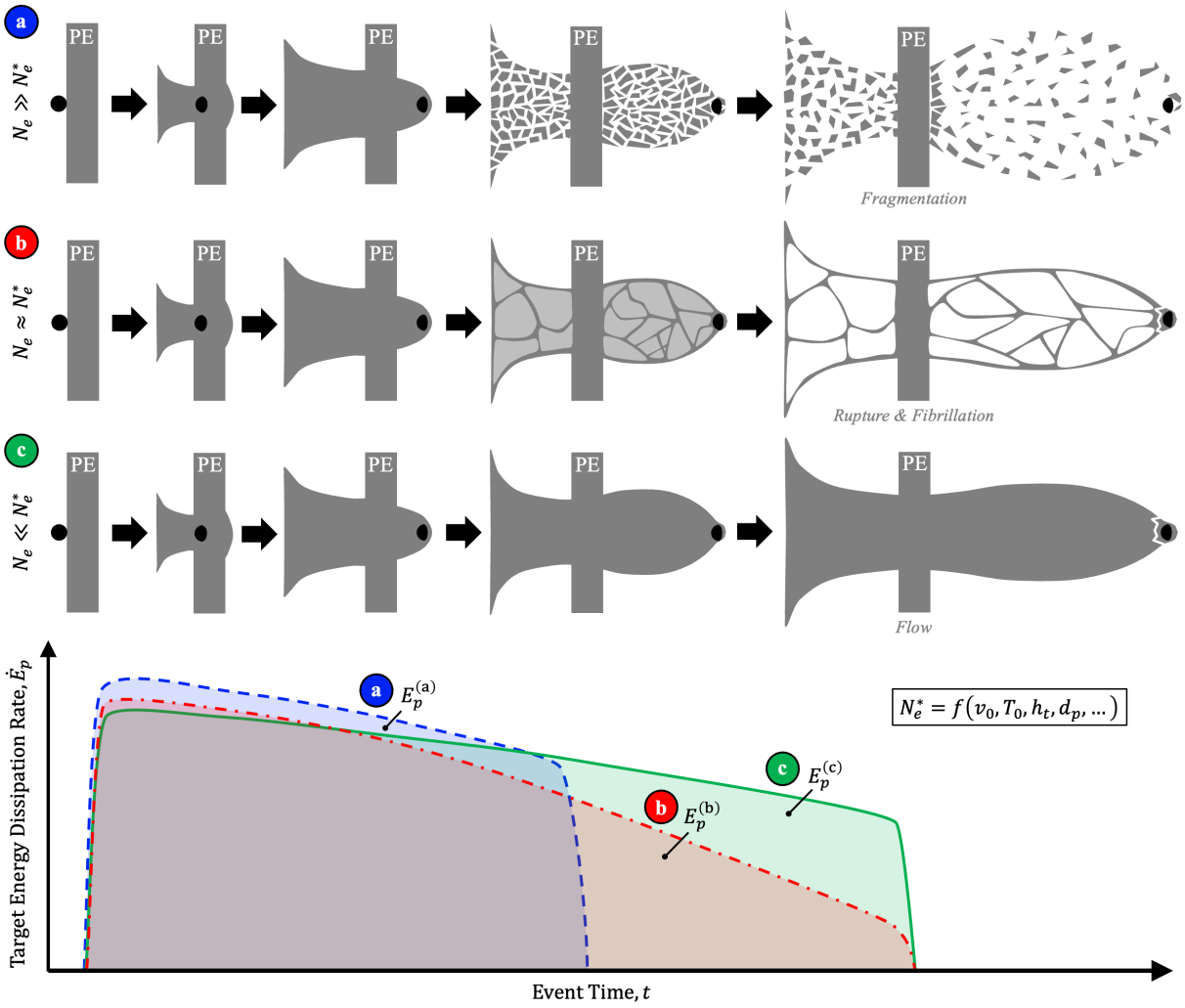


Figure 11: The effect of a PE's average number of entanglements per chain ($N_e$) on its primary failure modes when subjected to HVI: (1) at $N_e \gg N_e^*$, restricted molecular mobility leads to debris cloud fragmentation; (2) at $N_e \approx N_e^*$, a nonuniform membrane-like debris cloud forms, thins, and ruptures, resulting in an interconnected web-like network of PE fibrils; (3) at $N_e \ll N_e^*$, the decreased restriction on molecular mobility facilitates the formation of a membrane-like structure that can extensively expand without rupturing. The critical average number of entanglements per chain, $N_e^* = f(v_0, T_0, h_t, d_p, \ldots)$, marks the threshold at which the material shifts from predominantly bulk fragmentation to bulk flow. PEs with intermediate $N_e$ values display a mixture of these behaviors. Each bulk material failure mechanism initiates at a different event time, $t$, leading to variations in target energy absorption, $E_p = \int \dot{E}_p \, dt$, (*i.e.*, failed materials cease to dissipate energy).

longer the material remains intact during perforation, the more time energy dissipation mechanisms can operate (*i.e.*, increased $\tau$). Similarly, the more material that stays intact during perforation, the greater the proportion of deforming material that can dissipate energy (*i.e.*, enhanced $\dot{E}_p$).

For fixed $T_0$ and $\dot{\tilde{\varepsilon}}$, an impacted PE target will initially dissipate some energy through adiabatic shock heating, light emission, vaporization, and more, regardless of $N_e$. If $N_e \gg N_e^*$, the target continues to dissipate energy *via* rapid plastic work, thermal degradation, chain scission, and some local fracture before sudden widespread fragmentation of the deforming/flowing material causes a premature drop in $\dot{E}_p$ (Fig. 11a, $E_p^{(a)}$). For $N_e \approx N_e^*$, fragmentation does not occur; instead, the target absorbs more energy due

to increased thermal softening/melting and prolonged visco-plastic flow. The expanding material behaves like a membrane, prolonging interaction with the projectile and extending the impact time, $\tau$. As the material expands, it begins to experience rupture and fibrillation, leading to a gradual decrease in the target's instantaneous energy dissipation rate, $\dot{E}_p$, as more material fractures (Fig. 11b, $E_p^{(\mathrm{b})}$). When $N_e \ll N_e^*$, rupture is avoided, and $\dot{E}_p$ remains nonzero while the projectile interacts with the expanding, cooling, and stiffening PE material. Eventually, at a certain $\tau$, the projectile punctures the membrane, ceasing its interaction with the target (Fig. 11c, $E_p^{(\mathrm{c})}$).

As $N_e \to 0$ for the same impact conditions, the accompanying reduction in PE viscosity, strength, toughness, *etc.* begins to negate the improvements in $E_p$. Thus, there is an optimal $N_e$ value, $\hat{N}_e < N_e^*$, that maximizes $E_p$. For fixed $T_0$, a target impacted at $v_0^{(1)}$ will experience an average strain rate of $\dot{\bar{\varepsilon}}^{(1)}$. The target's energy absorption is maximum ($\max E_p^{(1)}$) when $N_e = \hat{N}_e^{(1)} < N_e^{*(1)}$. Another target of identical geometry impacted by the same projectile at $v_0^{(2)}$ will experience average strain rate $\dot{\bar{\varepsilon}}^{(2)}$. Its maximum energy absorption value ($\max E_p^{(2)}$) will be achieved at $N_e = \hat{N}_e^{(2)} < N_e^{*(2)}$. If $v_0^{(1)} > v_0^{(2)}$, then $\dot{\bar{\varepsilon}}^{(1)} > \dot{\bar{\varepsilon}}^{(2)}$ and $\hat{N}_e^{(1)} < \hat{N}_e^{(2)}$ (Fig. 12a and 12b). This $\hat{N}_e \propto 1/\dot{\bar{\varepsilon}}$ relationship is analogous to the time-temperature superposition principle exhibited by PE. In essence, increasing average strain rate requires a reduction in $N_e$ to sustain the degree of molecular mobility that leads to maximum $E_p$ (Fig. 12c).[14] This finding demonstrates the feasibility of a layered protective structure composed of $\mathcal{N}$ monolithic PE plates that is optimized for a specific impact threat envelope (*i.e.*, ranges of $v_0$, $d_p$, $m_p$, *etc.*). Given an envelope, $N_e$ of the $i$-th plate ($i = 1, 2, 3, \ldots, \mathcal{N}$) would be tuned to the optimal value ($\hat{N}_e^{(i)}$) specific to the local anticipated average strain rate ($\dot{\bar{\varepsilon}}^{(i)}$). Assuming the projectile impacts the $i = 1$ plate, $\dot{\bar{\varepsilon}}^{(i)}$ will decrease and $\hat{N}_e^{(i)}$ will increase as $i$ increases (Fig. 12d). In this way, each PE layer is designed for optimal energy absorption.

## 4. Conclusions

The declining efficacy of traditional spacecraft MMOD shields and military ballistic armor necessitates the development of layered, threat-optimized protective structures for HVI mitigation. UHMWPE and HDPE show promise as intermediate layers, owing to their high mass-specific energy absorption, tailorability, and low density and cost. While the relatively low-rate ($\dot{\varepsilon} < 10^3$ s$^{-1}$) behaviors of these PEs are well-documented, their responses to HVI-induced strain rates ($\dot{\varepsilon} > 10^6$ s$^{-1}$) are virtually unexplored and not well understood, especially near their $T_g$ and $T_m$ values. This study investigated the interplay of $T_0$, $v_0$, and $N_e$ on PE's HVI response to help address fundamental questions about its dynamic behavior and highlight its engineering applications. 12.7 mm thick UHMWPE ($M_w = 4.7 \times 10^6$ g/mol, $N_e \sim 3,800$) and HDPE

[14] Since $T_0$ increases molecular mobility, $\hat{N}_e \propto T_0$.

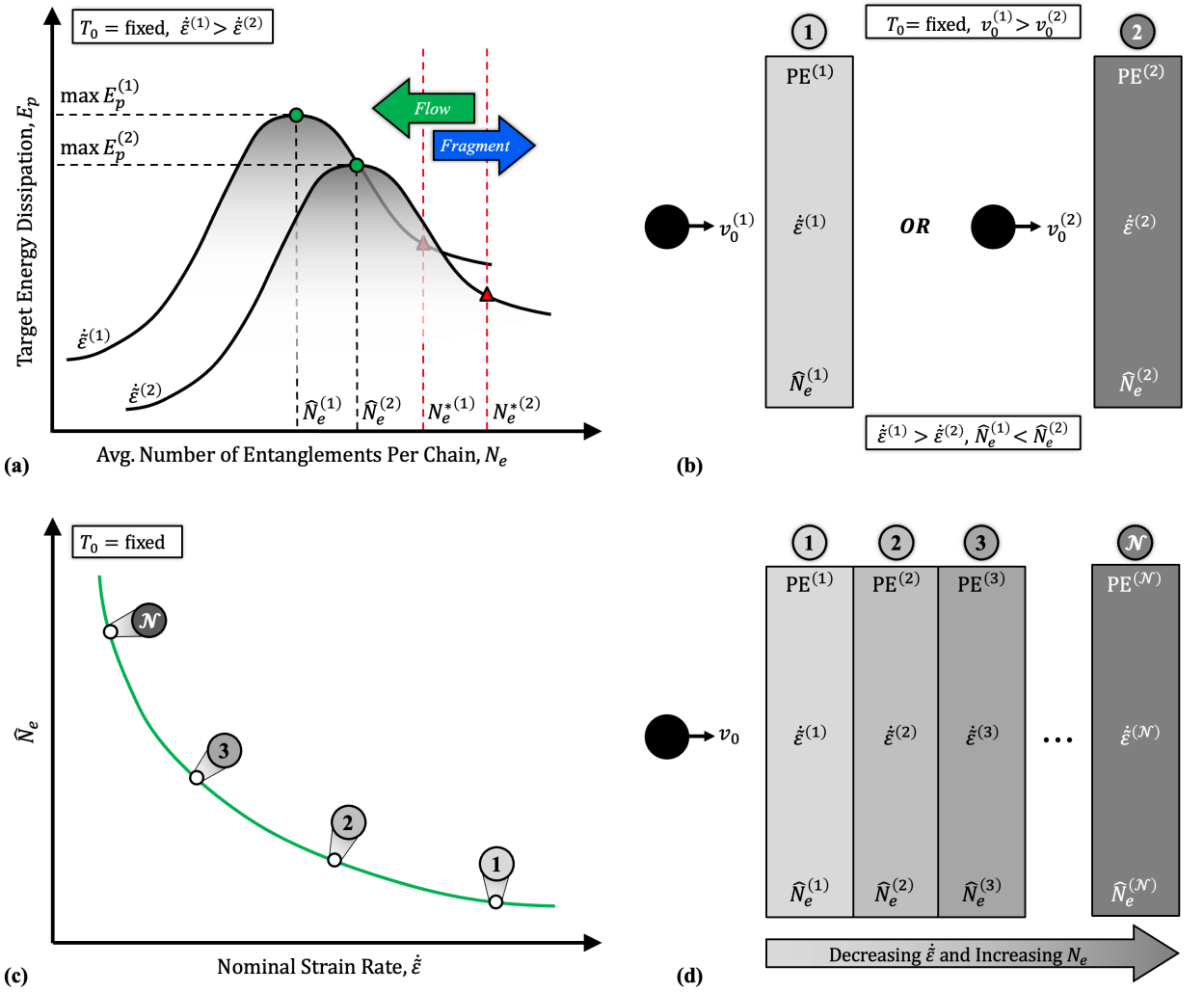


Figure 12: PE target energy absorption optimization: (a, b) the number of entanglements resulting in maximum $E_p$ ($\hat{N}_e$) decreases with increasing $v_0$ and thus average strain rate ($\dot{\bar{\varepsilon}}$). $\hat{N}_e$ is less than $N_e^* = f(T_0, \dot{\bar{\varepsilon}}, \dots)$, the $N_e$ value defining PE's transition from bulk quasi-brittle fragmentation to large-scale plastic deformation/flow at a given $v_0$, $T_0$, and projectile-target combination. (c) For fixed $T_0$, $\hat{N}_e$ decreases with increasing average strain rate. (d) A layered PE plate protective structure where, give a threat envelope ($v_0$, $d_p$, ...), each $i$-th layer ($i = 1, 2, 3, \dots, \mathcal{N}$) is tuned to dissipate the maximum energy for its local anticipated average strain rate. The plates are chosen to be more entangled as strain rate decreases.

($M_w = 1.7 \times 10^5$ g/mol, $N_e \sim 140$) plates were subjected to 2.5 km/s and 6.0 km/s HVIs by 6.35 mm diameter 2017-T4 aluminum spheres. Targets were impacted at $T_0 \approx -120$°C, 20°C, and 140°C.

Pre-impact, *in-situ*, and post-impact results together affirm that differences in deformation behavior, failure modes, and relative energy absorption between the two PEs can be attributed to a competition between average rates of loading and chain relaxation. At $T_0 \approx -120$°C, both HDPE targets showed extensive cracking and fragmented completely. Conversely, the UHMWPE samples resisted widespread cracking but developed cone cracks around their perforations that generated large annular spall fragments. Debris clouds for both $-120$°C PE plates were populated with distinct target fragments. At room temperature,

the UHMWPE targets fragmented extensively, whereas HDPE samples underwent significant thermal softening/melting and visco-plastic flow. UHMWPE debris clouds consisted of distinct fragments, while HDPE debris clouds were akin to expanding, web-like networks of interconnected molten fibrils, observations consistent with previous work. Heating the UHMWPE targets to 140°C increased the amount of flowing/molten material in the debris clouds. Yet, this enhanced flow ultimately gave way to widespread melt fracture, resulting in bulk UHMWPE fragmentation even when impacted above its $T_m$. The 140°C HDPE samples instead exhibited increased high-rate softening, melting, and flow without fracturing, leading to the formation of membrane-like debris clouds that underwent extreme expansion without rupture. All targets exhibited charring and discoloration indicative of thermal degradation from impact-induced heating, in line with predictions. In general, lowering $T_0$ for fixed $N_e$ inhibited high-rate chain motion analogously to increasing $N_e$ at fixed $T_0$, making HDPE behave more like UHMWPE when subjected to similar HVIs. The opposite was also observed. Increasing $v_0$ heightened fracture/fragmentation susceptibility in both PEs by elevating strain rates beyond their rates of chain disentanglement and reorientation. The PE that lost less mass, had smaller perforations, and better absorbed energy generally exhibited the most visco-plastic flow without subsequent bulk fragmentation.

These observations suggest a critical $N_e$ value exists, which, given constant $v_0$, $T_0$, and projectile-target combination, marks a PE target's HVI response shift from widespread fragmentation to bulk thermal softening/melting and flow. Consequently, for the same impact conditions, there is an optimal $N_e$ value that maximizes PE target energy absorption. Raising $v_0$ or lowering $T_0$ necessitates a decrease in $N_e$ to maintain the molecular mobility essential for optimal energy absorption. Hence, a layered, strain-rate-tuned PE protective structure is viable.

## Acknowledgments

This research is based upon work partially supported by the National Science Foundation Graduate Research Fellowship under Grant No. 1746932. The views and conclusions contained in this document are those of the authors and should not be interpreted as representing the official policies, either expressed or implied, of the Army Research Office or the U.S. Government. The U.S. Government is authorized to reproduce and distribute reprints for Government purposes notwithstanding any copyright notation herein.

## References

[1] E. L. Christiansen, "Meteoroid/debris shielding," National Aeronautics and Space Administration, Lyndon B. Johnson Space ..., Tech. Rep., 2003.

[2] E. L. Christiansen *et al.*, "Handbook for designing mmod protection," *NASA Johnson Space Center, NASA/TM-2009-214785*, 2009.

[3] H. M. Sayler, *Hypersonic weapons: Background and issues for Congress.* Congressional Research Service, 2019.

[4] R. O'Rourke, "Navy lasers, railgun, and hypervelocity projectile: Background and issues for congress," *Congressional Research Service*, vol. 17, 2017.

[5] J. M. Acton, "Hypersonic boost-glide weapons," *Science & Global Security*, vol. 23, no. 3, pp. 191–219, 2015.

[6] J. D. Walker, *Modern impact and penetration mechanics*. Cambridge university press, 2021.

[7] J. D. Walker, "From columbia to discovery: Understanding the impact threat to the space shuttle," *International journal of impact engineering*, vol. 36, no. 2, pp. 303–317, 2009.

[8] W. P. Schonberg *et al.*, "Hypervelocity impact physics," NASA, Tech. Rep., 1991.

[9] S. Signetti and A. Heine, "Transition regime between high-velocity and hypervelocity impact in metals–a review of the relevant phenomena for material modeling in ballistic impact studies," *International Journal of Impact Engineering*, vol. 167, p. 104 213, 2022.

[10] J. A. Rogers *et al.*, "The pursuit of hypervelocities: A review of two-stage light gas gun aeroballistic ranges," *International Journal of Impact Engineering*, p. 104 861, 2023.

[11] R. Thirsk *et al.*, "The space-flight environment: The international space station and beyond," *Cmaj*, vol. 180, no. 12, pp. 1216–1220, 2009.

[12] Y. Zhao *et al.*, "Global patterns of hottest, coldest, and extreme diurnal variability on earth," *Bulletin of the American Meteorological Society*, vol. 102, no. 9, E1672–E1681, 2021.

[13] O. Uyanna and H. Najafi, "Thermal protection systems for space vehicles: A review on technology development, current challenges and future prospects," *Acta Astronautica*, vol. 176, pp. 341–356, 2020.

[14] E. Christiansen *et al.*, "Enhanced meteoroid and orbital debris shielding," *International Journal of Impact Engineering*, vol. 17, no. 1-3, pp. 217–228, 1995.

[15] J. Moonen *et al.*, "Evaluating UHMWPE-stuffed aluminium foam sandwich panels for protecting spacecraft against micrometeoroid and orbital debris impact," *International Journal of Impact Engineering*, vol. 180, p. 104 668, 2023.

[16] M. Jacobs and J. Van Dingenen, "Ballistic protection mechanisms in personal armour," *Journal of materials science*, vol. 36, no. 13, pp. 3137–3142, 2001.

[17] N. Kawai *et al.*, "In-situ observation of damage evolution in polycarbonate subjected to hypervelocity impact," *International Journal of Impact Engineering*, vol. 142, p. 103 584, 2020.

[18] K. Qu *et al.*, "Ballistic performance of multi-layered aluminium and uhmwpe fibre laminate targets subjected to hypervelocity impact by tungsten alloy ball," *Composite Structures*, vol. 253, p. 112 785, 2020.

[19] S. Khatiwada *et al.*, "Hypervelocity impact experiments on epoxy/ultra-high molecular weight polyethylene fiber composites reinforced with single-walled carbon nanotubes," *Procedia Engineering*, vol. 58, pp. 4–10, 2013.

[20] N Kawai *et al.*, "Stress wave and damage propagation in transparent materials subjected to hypervelocity impact," *Procedia Engineering*, vol. 103, pp. 287–293, 2015.

[21] K. Callahan *et al.*, "High strain rate failure behavior of polycarbonate plates due to hypervelocity impact," *Macromolecules*, vol. 55, no. 21, pp. 9640–9649, 2022.

[22] A. Kozhushko and A. Sinani, "Hypervelocity impact for brittle targets," *International journal of impact engineering*, vol. 29, no. 1-10, pp. 391–396, 2003.

[23] J. A. Rogers *et al.*, "Hypervelocity impact response of monolithic UHMWPE and HDPE plates," *International Journal of Impact Engineering*, vol. 161, p. 104 081, 2022.

[24] J.-H. Cha *et al.*, "Ultra-high-molecular-weight polyethylene as a hypervelocity impact shielding material for space structures," *Acta Astronautica*, vol. 168, pp. 182–190, 2020.

[25] K Ohtani *et al.*, "A study of hypervelocity impact on cryogenic materials," *International journal of impact engineering*, vol. 33, no. 1-12, pp. 555–565, 2006.

[26] D. Numata *et al.*, "Hvi tests on cfrp laminates at low temperature," *International Journal of Impact Engineering*, vol. 35, no. 12, pp. 1695–1701, 2008.

[27] B. Wells, "Hypervelocity impact tests on coated thermoplastic films at cryogenic and elevated temperatures," *International journal of impact engineering*, vol. 33, no. 1-12, pp. 855–861, 2006.

[28] W. Xie *et al.*, "High velocity impact tests on high temperature carbon-carbon composites," *Composites Part B: Engineering*, vol. 98, pp. 30–38, 2016.

[29] C. R. Siviour and J. L. Jordan, "High strain rate mechanics of polymers: A review," *Journal of Dynamic Behavior of Materials*, vol. 2, pp. 15–32, 1 Mar. 2016, ISSN: 21997454. DOI: 10.1007/s40870-016-0052-8.

[30] I. Mohagheghian *et al.*, "Impact perforation of monolithic polyethylene plates: Projectile nose shape dependence," *International Journal of impact engineering*, vol. 80, pp. 162–176, 2015.

[31] J. M. Kelly, "Ultra-high molecular weight polyethylene," *Journal of Macromolecular Science, Part C: Polymer Reviews*, vol. 42, no. 3, pp. 355–371, 2002.

[32] S. M. Aharoni, "Correlations between chain parameters and failure characteristics of polymers below their glass transition temperature," *Macromolecules*, vol. 18, no. 12, pp. 2624–2630, 1985.

[33] A. M. Donald and E. J. Kramer, "Effect of molecular entanglements on craze microstructure in glassy polymers," *Journal of Polymer Science: Polymer Physics Edition*, vol. 20, no. 5, pp. 899–909, 1982.

[34] P. G. Whitten and H. R. Brown, "Polymer entanglement density and its influence on interfacial friction," *Physical Review E*, vol. 76, no. 2, p. 026 101, 2007.

[35] P. C. Painter and M. M. Coleman, *Essentials of polymer science and engineering*. Lancaster, Pennsylvania: DEStech Publications, Inc., 2009.

[36] M. M. Xu *et al.*, "Static and dynamic properties of semi-crystalline polyethylene," *Polymers*, vol. 8, 4 2016, ISSN: 20734360. DOI: 10.3390/polym8040077.

[37] J.-F. Agassant *et al.*, *Polymer processing: principles and modeling*. Carl Hanser Verlag GmbH Co KG, 2017.

[38] R. K. Krishnaswamy *et al.*, "Effect of the distribution of short-chain branches on crystallization kinetics and mechanical properties of high-density polyethylene," *Macromolecules*, vol. 41, no. 5, pp. 1693–1704, 2008.

[39] B. Bersted, "On the effects of very low levels of long chain branching on rheological behavior in polyethylene," *Journal of applied polymer science*, vol. 30, no. 9, pp. 3751–3765, 1985.

[40] E. Brown *et al.*, "Influence of molecular conformation on the constitutive response of polyethylene: A comparison of HDPE, UHMWPE, and PEX," *Experimental Mechanics*, vol. 47, no. 3, pp. 381–393, 2007.

[41] S Austin *et al.*, "The high-velocity impact of dyneema® and spectra® laminates: Implementation of a simple thermal softening model," *Procedia Engineering*, vol. 204, pp. 51–58, 2017.

[42] A. I. Mourad *et al.*, "Ultra high molecular weight polyethylene deformation and fracture behaviour as a function of high strain rate and triaxial state of stress," *International Journal of Fracture*, vol. 120, no. 3, pp. 501–515, 2003.

[43] E. Brown *et al.*, "Influence of polyethylene molecular conformation on taylor impact measurements: A comparison of HDPE, UHMWPE, and PEX," in *AIP Conference Proceedings*, American Institute of Physics, vol. 955, 2007, pp. 691–694.

[44] J. Furmanski *et al.*, "Time–temperature equivalence and adiabatic heating at large strains in high density polyethylene and ultrahigh molecular weight polyethylene," *Polymer*, vol. 54, no. 1, pp. 381–390, 2013, ISSN: 0032-3861. DOI: https://doi.org/10.1016/j.polymer.2012.11.010.

[45] R. W. Nunes *et al.*, "Influence of molecular weight and molecular weight distribution on mechanical properties of polymers," *Polymer Engineering & Science*, vol. 22, no. 4, pp. 205–228, 1982.

[46] J Karger-Kocsis *et al.*, "Effects of molecular weight on the perforation impact behavior of injection-molded plaques of $\alpha$-and $\beta$-phase isotactic polypropylenes," *Journal of Macromolecular Science—Physics*, vol. 38, no. 5-6, pp. 647–662, 1999.

[47] A Van der Wal *et al.*, "Fracture of polypropylene: The effect of crystallinity," *Polymer*, vol. 39, no. 22, pp. 5477–5481, 1998.

[48] B. Li *et al.*, "Influence of molecular weight on impact fracture behavior of injection molded high density polyethylene: Scanning electron micrograph observations," *Journal of applied polymer science*, vol. 109, no. 2, pp. 1161–1167, 2008.

[49] I Brough *et al.*, "Scanning electron micrographs of high density polyethylene fracture surfaces," *Polymer*, vol. 45, no. 10, pp. 3115–3123, 2004.

[50] N. Brooks *et al.*, "Effects of morphology on the yield stress of polyethylene," *Polymer*, vol. 40, no. 4, pp. 821–825, 1999, ISSN: 0032-3861. DOI: https://doi.org/10.1016/S0032-3861(98)00324-3.

[51] B. A. Schrauwen *et al.*, "Intrinsic deformation behavior of semicrystalline polymers," *Macromolecules*, vol. 37, no. 16, pp. 6069–6078, 2004.

[52] C. Price, "Influence of thermal and dynamic viscoelastic properties of polymers on low-mass, high-velocity penetrations," M.S. thesis, Mississippi State University, 2016.

[53] I.-C. Yeh *et al.*, "Mechanical and structural characterization of semicrystalline polyethylene under tensile deformation by molecular dynamics simulations," *Macromolecules*, vol. 48, no. 12, pp. 4228–4239, 2015.

[54] S. Lee and G. C. Rutledge, "Plastic deformation of semicrystalline polyethylene by molecular simulation," *Macromolecules*, vol. 44, no. 8, pp. 3096–3108, 2011.

[55] D Hossain *et al.*, "Molecular dynamics simulations of deformation mechanisms of amorphous polyethylene," *Polymer*, vol. 51, no. 25, pp. 6071–6083, 2010.

[56] M. Bowering, "Strain rate effects on energy dissipation during hypervelocity penetration of polymeric materials," M.S. thesis, Mississippi State University, 2018.

[57] Y. Sui *et al.*, "Eminent differences in cryogenic toughness of ultra-high molecular weight polyethylene with different entanglement densities," *Journal of Applied Polymer Science*, vol. 140, no. 7, e53475, 2023.

[58] M. Amjadi and A. Fatemi, "Tensile behavior of high-density polyethylene including the effects of processing technique, thickness, temperature, and strain rate," *Polymers*, vol. 12, no. 9, p. 1857, 2020.

[59] I. I. Salakhov *et al.*, "Low-temperature mechanical properties of high-density and low-density polyethylene and their blends," *Polymers*, vol. 13, no. 11, p. 1821, 2021.

[60] L. Fetters *et al.*, "Connection between polymer molecular weight, density, chain dimensions, and melt viscoelastic properties," *Macromolecules*, vol. 27, no. 17, pp. 4639–4647, 1994.

[61] *TIVAR® 1000 virgin UHMW-PE: Product datasheet*, Mitsubishi Chemical Advanced Materials, Reading, PA. [Online]. Available: `https://www.mcam.com/na-en/products/engineering-plastics/standard/tivarr-uhmw-pe-family-of-products/tivarr-1000/`.

[62] *King Performance Commodities HDPE: material and physical datasheet*, King Plastic Corporation, North Port, FL, 2014. [Online]. Available: `https://www.kingplastic.com/wp-content/uploads/2014/05/King-KPC-HDPE-Physical-Properties.pdf`.

[63] D. Jauffres *et al.*, "Microstructural origin of physical and mechanical properties of ultra high molecular weight polyethylene processed by high velocity compaction," *Polymer*, vol. 48, no. 21, pp. 6374–6383, 2007.

[64] J. Min *et al.*, "Development of synthetic resin-based mortar for low-activation and neutron shields," *Construction and Building Materials*, vol. 124, pp. 992–998, 2016.

[65] C. Zhang *et al.*, "High elastic modulus polyethylene–a two-stage multi-axial rolling and orientation process," *Polymer*, vol. 256, p. 125 180, 2022.

[66] K. Patel *et al.*, "Ultrahigh molecular weight polyethylene: Catalysis, structure, properties, processing and applications," *Progress in polymer science*, vol. 109, p. 101 290, 2020.

[67] V. Litvinov *et al.*, "Chain entanglements in polyethylene melts. why is it studied again?" *Macromolecules*, vol. 46, no. 2, pp. 541–547, 2013.

[68] L. J. Fetters *et al.*, "Packing length influence in linear polymer melts on the entanglement, critical, and reptation molecular weights," *Macromolecules*, vol. 32, no. 20, pp. 6847–6851, 1999.

[69] J. A. Rogers *et al.*, "The texas a&m university hypervelocity impact laboratory: A modern aeroballistic range facility," *Review of Scientific Instruments*, vol. 93, no. 8, 2022.

[70] G. R. Johnson, "Analysis of Elastic-Plastic Impact Involving Severe Distortions," *Journal of Applied Mechanics*, vol. 43, no. 3, pp. 439–444, Sep. 1976, ISSN: 0021-8936. DOI: `10.1115/1.3423887`.

[71] G. R. Johnson *et al.*, "An algorithm to automatically convert distorted finite elements into meshless particles during dynamic deformation," *International Journal of Impact Engineering*, vol. 27, no. 10, pp. 997–1013, 2002.

[72] E. Grüneisen, "Theorie des festen zustandes einatomiger elemente," *Annalen der Physik*, vol. 344, no. 12, pp. 257–306, 1912.

[73] G. R. Johnson, "A constitutive model and data for materials subjected to large strains, high strain rates, and high temperatures," *Proc. 7th Inf. Sympo. Ballistics*, pp. 541–547, 1983.

[74] G. R. Johnson and W. H. Cook, "Fracture characteristics of three metals subjected to various strains, strain rates, temperatures and pressures," *Engineering fracture mechanics*, vol. 21, no. 1, pp. 31–48, 1985.

[75] J. Rogers *et al.*, "Simulating hypervelocity impacts to high-density polyethylene," in *AIAA SCITECH 2023 Forum*, 2023, p. 2021.

[76] W. Herrmann and J. S. Wilbeck, "Review of hypervelocity penetration theories," *International Journal of Impact Engineering*, vol. 5, no. 1-4, pp. 307–322, 1987.

[77] S. Morye *et al.*, "Modelling of the energy absorption by polymer composites upon ballistic impact," *Composites science and technology*, vol. 60, no. 14, pp. 2631–2642, 2000.

[78] R. C. Huber *et al.*, "In situ x-ray diffraction of high density polyethylene during dynamic drive: Polymer chain compression and decomposition," *Journal of Applied Physics*, vol. 130, no. 17, 2021.

[79] M. E. Backman and W. Goldsmith, "The mechanics of penetration of projectiles into targets," *International Journal of Engineering Science*, vol. 16, no. 1, pp. 1–99, 1978.

[80] H. Yang *et al.*, "Thermal, rheological, and mechanical characterization of compression and injection molded ultra-high molecular weight polyethylene, high density polyethylene, and their blends," *Journal of Applied Polymer Science*, vol. 140, no. 7, e53484, 2023.

# Supplementary Information for

Temperature Dependence of the Hypervelocity Impact Response of Polyethylene Plates from $T_g$ to $T_m$

Jacob A. Rogers *et al.*

## SI. Supplementary Information

### *SI.1. Target Boundary Considerations*

In-plane reflected waves from the target's boundary, influenced by the materials, shapes, and relative impact velocity of the projectile and target, can affect the dynamics of penetration and/or perforation. If the time taken for perforation ($t_p$) is significantly shorter than the duration for the leading shock wave to travel from the impact point to the boundary and back ($t_b$), disruption of the perforation event from reflected waves is unlikely. Hence, evaluating the ratio $t_p/t_b$ offers insight into potential boundary effects.

The time for a shock wave to travel to the boundary and back in a given axisymmetric target can be estimated as

$$t_b \approx 2\frac{r_b}{U_t}, \tag{S1}$$

where $r_b$ is the in-plane radius from the impact point to the target boundary and $U_t$ is the shock velocity (a function of $v_0$). For simplicity, this analysis of boundary effects only considers HDPE as the target material, but the results would be similar for UHMWPE. $U_t$ values for HDPE were sourced and extrapolated from Ref. [1]. Similarly, noting that $v_{dc}/v_0 \lessapprox 0.5$ for the experiments in this study, the perforation/puncture time can be approximated as

$$t_p \approx \frac{2h_t}{v_0 + v_r} \approx \frac{2h_t}{v_0 + v_{dc}} \approx \frac{4}{3}\frac{h_t}{v_0}, \tag{S2}$$

where $h_t$ is the target thickness, $v_0$ is the projectile impact velocity, and $v_r \sim v_{dc}$ is the projectile residual velocity after impact. For all experiments, $r_b = 3.8$ cm. Using $v_0$ values that span the tested range ($v_0 = 2.0$–$6.5$ km/s), values for $t_b$, $t_p$, and $t_p/t_b$ were approximated (Table S1). These simple calculations show that for all impacts, the perforation time was much less than the wave travel time ($t_p \lesssim 0.5t_b$), indicating reflected in-plane waves did not influence experimental perforation dynamics.

### *SI.2. Simple Two-Dimensional Heat Transfer Simulations for the PE Plates*

2D heat transfer simulations in the fast-running Energy2D multi-physics software (version 3.0.3) [2] were used to estimate how the difference in the PE target's mid-plane ($T_2$) and surface ($T_1$) temperatures temporally evolved as it warmed and cooled. Energy2D combines fast finite-difference algorithms and a computational fluid dynamics (CFD) engine to solve the heat equation and the Navier-Stokes equation. Given that the PEs had similar thermal properties, only two simulations were run: one for $T_0 = -180$°C (warming) and one for $T_0 = 170$°C (cooling). Each simulated plate's cross-sectional dimensions (102 mm x

Table S1: Approximations of wave travel time ($t_b$), perforation time ($t_p$), and their ratio ($t_p/t_b$) for the PE sample geometry and fixturing. Calculated values are based on the target's approximate shock velocity ($U_t$), projectile impact and residual velocities ($v_0$ and $v_r \sim v_{dc}$), and in-plane radius from the impact point to the boundary ($r_b$). The analysis shows that for all impacts, the perforation time is significantly shorter than the wave travel time.

| No. | $v_0$ (km/s) | $v_{dc}$ (km/s) | $h_t$ (mm) | $t_p$ (µs) | $r_b$ (cm) | $t_b$ (µs) | $t_p/t_b$ (%) |
|---|---|---|---|---|---|---|---|
| 1 | 2.00 | 1.00 | 12.7 | 8.47 | 3.81 | 13.1 | 64 |
| 2 | 2.50 | 1.25 | 12.7 | 6.77 | 3.81 | 12.7 | 53 |
| 3 | 3.00 | 1.50 | 12.7 | 5.64 | 3.81 | 11.6 | 49 |
| 4 | 3.50 | 1.75 | 12.7 | 4.84 | 3.81 | 10.7 | 45 |
| 5 | 4.00 | 2.00 | 12.7 | 4.23 | 3.81 | 9.9 | 43 |
| 6 | 4.50 | 2.25 | 12.7 | 3.76 | 3.81 | 9.2 | 41 |
| 7 | 5.00 | 2.50 | 12.7 | 3.39 | 3.81 | 8.6 | 39 |
| 8 | 5.50 | 2.75 | 12.7 | 3.08 | 3.81 | 8.1 | 38 |
| 9 | 6.00 | 3.00 | 12.7 | 2.82 | 3.81 | 7.6 | 37 |
| 10 | 6.50 | 3.25 | 12.7 | 2.61 | 3.81 | 7.2 | 36 |

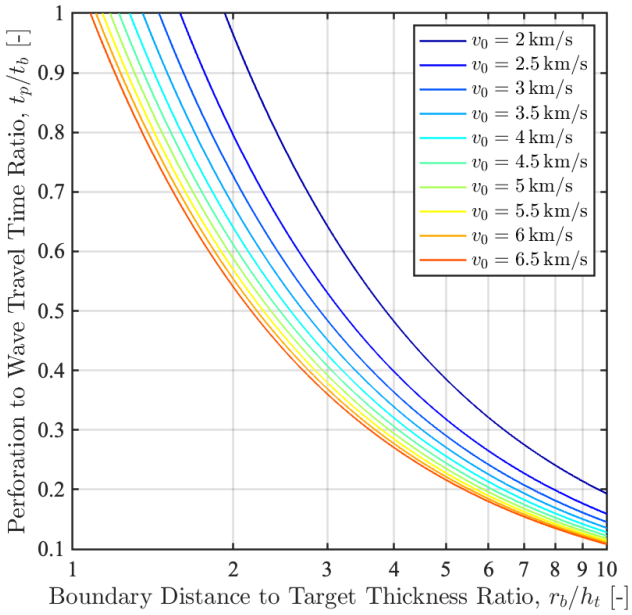


Figure S1: The effect of target-center-to-boundary distance ($r_b$) and target thickness ($h_t$) on the projectile perforation time ($t_p$) compared to the longitudinal stress wave travel time ($t_b$) across various impact velocities ($v_0$). The projectile size is assumed significantly smaller than the distance from target center to boundary ($d_p \ll r_b$).

12.7 mm) matched those from the HVI experiments. The representative plate's thermal conductivity, specific heat capacity, and density were assigned values of 0.5 W/(K·m), 2.0 kJ/(kg·K), and 0.93 g/cm$^3$, respectively (*cf.* Table 1 in main document). The warming/cooling process was simulated for twenty minutes, with a time step of 0.01 seconds. The plates were isolated in a 250 mm x 250 mm "volume" lab air at $T_\infty = 20°$C, which was descritized into a 100 x 100 square computation grid. For each plate, the difference between $T_2$ and $T_1$ varied over time but averaged around 6°C, with a standard deviation of about 0.7°C (Fig. S2a). Figures S2b and S2c present snapshots of the temperature fields around the targets, each taken about one minute into the simulation. The denser cold air flows downward, while the hotter air flows upward, due to gravity.

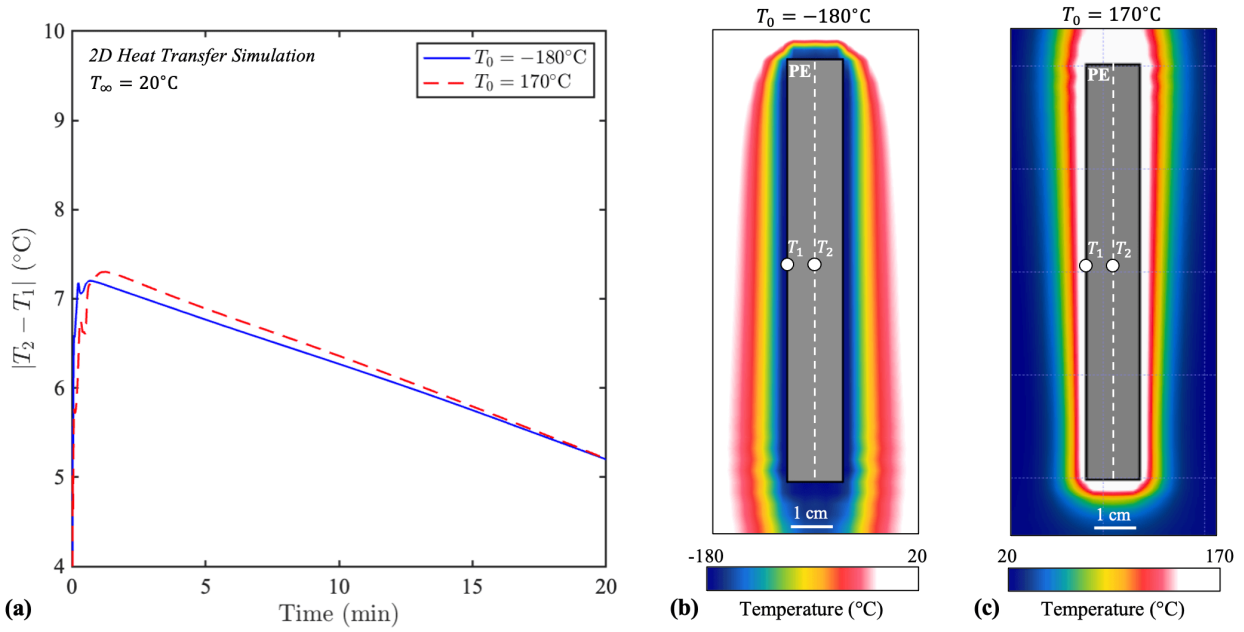


Figure S2: 2D heat transfer simulation results for a representative PE plate: (a) Displays the temperature differences between the target mid-plane ($T_2$) and surface ($T_1$) over time for $T_0 = -180$°C and $T_0 = 170$°C. For both $T_0$, $|T_2 - T_1|$ averaged approximately 6°C with a standard deviation of 0.7°C. (b) and (c) Present snapshots of the temperature field surrounding the targets, both at approximately one minute into the simulation.

### *SI.3. An Energy-Based Debris Cloud Lethality Comparison Metric*

During a HVI, the projectile's kinetic energy is absorbed through intense deformation, erosion, fracture, fragmentation, heating, melting, vaporization, and sometimes sublimation of both projectile and target. An ejecta cloud usually forms at the impact face of the target, moving "uprange" (*cf.* Fig. 2) in the opposite direction to the projectile [3, 4]. When perforation occurs, a debris cloud composed largely of melted or solid target material fragments, plus the projectile or its fragments,[15] emerges and expands "downrange" from the target's exit side. In non-perforating cratering events, only an ejecta cloud forms. Determining the projectile momentum and kinetic energy absorbed by the target requires resolving the three-dimensional (3D) momenta and kinetic energies of all fragments in the ejecta and debris clouds. This is a challenging task, as differentiating between projectile and target fragments in these clouds is nontrivial, even with advanced diagnostics. Additionally, even if a fragment's origin is identified, assumptions about its mass, material state, and 3D geometry would still be required.

In most practical HVI shielding applications, important assets or personnel are located on the downrange side of the target, where the debris cloud forms and expands. Therefore, numerous studies comparing the HVI performance of different materials have focused on examining the debris cloud and its potential lethality [5–

[15] Vaporized material from the projectile or target may be present in the debris cloud but likely has negligible contribution to the debris cloud's kinetic energy due to its low mass.

10]. This approach is particularly used in the development of spacecraft protective structures (*i.e.*, Whipple shields). One way to evaluate the lethality of a debris cloud is through conservative total kinetic energy arguments. For a given HVI event, the energy balance can be expressed as

$$E_0 = \frac{1}{2} m_p v_0^2 = E_{ec} + E_{dc} + E_l, \tag{S3}$$

where $E_{ec}$ and $E_{dc}$ represent the total kinetic energy of the ejecta and debris cloud, respectively, and $E_l$ is the energy dissipated through plastic work, shocking heating, fracture, phase change, *etc.* of projectile/target material. In the following discussion, debris cloud fragment rotational kinetic energy is considered negligible. Furthermore, the debris cloud is considered to be axisymmetric about the impact axis, which is typical for isotropic projectiles striking isotropic targets at normal incidence.[16] Consequently, the total kinetic energy of the debris cloud is the sum of each distinct fragment's translational kinetic energy, *i.e.*,

$$E_{dc} = \frac{1}{2} \left( \sum_{i=1}^{N_p} m_{p,dc}^i (\boldsymbol{v}_{p,dc}^i \cdot \boldsymbol{v}_{p,dc}^i) + \sum_{i=1}^{N_t} m_{t,dc}^i (\boldsymbol{v}_{t,dc}^i \cdot \boldsymbol{v}_{t,dc}^i) \right), \tag{S4}$$

where $m_{p,dc}^i$ and $\boldsymbol{v}_{p,dc}^i$ represent the mass and velocity of the $i$-th *projectile* fragment, and $m_{t,dc}^i$ and $\boldsymbol{v}_{t,dc}^i$ those of the $i$-th *target* fragment in the debris cloud. $N_p$ and $N_t$ are the total counts of distinct projectile and target fragments, respectively. Projectile and target fragments travel downrange at flight angles $\theta_p^i$ and $\theta_t^i$, respectively, both ranging from $0^\circ$ to $90^\circ$ relative to the impact axis. A fragment's velocity magnitude is generally inversely proportional to its flight angle. Hence, the total kinetic energy of the projectile fragments in the debris cloud is bounded by that of their combined mass moving directly downrange ($\theta_p^i = 0$, for all $i \in \{1, 2, \ldots, N_p\}$) at the measurable debris cloud tip velocity $v_{dc}$:

$$\sum_{i=1}^{N_p} m_{p,dc}^i (\boldsymbol{v}_{p,dc}^i \cdot \boldsymbol{v}_{p,dc}^i) \leq \alpha m_p v_{dc}^2 \leq m_p v_{dc}^2, \tag{S5}$$

where the ratio $0 \leq \alpha \leq 1$ represents the level of projectile contribution to $E_{dc}$. Likewise, the target fragments in the debris cloud predominantly move in the direction of projectile motion, each at some fraction of $v_{dc}$. Hence, the upper limit of their total kinetic energy is the same as if their total mass were moving together

[16] This discussion can be expanded to include oblique HVIs by accounting for the impact angle, though normal impacts are typically the most severe.

downrange ($\theta_t^i = 0$, for all $i \in \{1, 2, \ldots, N_t\}$) at velocity $v_{dc}$:

$$\sum_{i=1}^{N_t} m_{t,dc}^i (\boldsymbol{v}_{t,dc}^i \cdot \boldsymbol{v}_{t,dc}^i) = \beta M_{t,dc} v_{dc}^2 \leq M_{t,dc} v_{dc}^2, \tag{S6}$$

where $M_{t,dc}$ is the total mass of the target fragments in the debris cloud and $0 \leq \beta \leq 1$ represents the level of target contribution to $E_{dc}$. The mass $M_{t,dc}$ can be estimated by $M_{t,dc} \approx \gamma \Delta m_t$, where $0 \leq \gamma \leq 1$ represents the proportion of the target's impact-induced mass loss present in the debris cloud.

Normalizing Eq. (S3) by projectile impact energy ($E_0 = \frac{1}{2} m_p v_0^2$), substituting in Eqs. (S4)–(S6), and rearranging yields

$$\left(\alpha + \zeta \frac{\Delta m_t}{m_p}\right) \frac{v_{dc}^2}{v_0^2} + \frac{1}{E_0} \left(E_{ec} + E_l\right) \leq 1, \tag{S7}$$

where $0 \leq \zeta = \beta\gamma \leq 1$ indicates the target's overall contribution to $E_{dc}$ and the inequality arises due to the exclusion of fragment rotational kinetic energy. In the worst-case scenario with $\alpha = 1$ and $\zeta = 1$, all of the projectile's mass ($m_p$) and the target's lost mass ($\Delta m_t$) are concentrated in the debris cloud, moving downrange at velocity $v_{dc}$:

$$\frac{E_{dc,max}}{E_0} = \left(1 + \frac{\Delta m_t}{m_p}\right) \frac{v_{dc}^2}{v_0^2}. \tag{S8}$$

For fixed projectile mass and impact velocity, the debris cloud tip velocity required to maintain a given lethality level ($E_{dc}/E_0$ value) intuitively decreases as target mass loss increases (Fig. S3a). Conversely, $\zeta = 0$ indicates that only the projectile or its fragments move downrange with kinetic energy $\frac{1}{2}\alpha m_p v_{dc}^2$. No perforation occurs if both $\alpha = 0$ and $\zeta = 0$, and $E_{ec} + E_l$ is maximum. If the projectile remains *completely* intact, $\alpha = 1$ and Eq. (S7) can be rewritten as

$$E_p \approx \frac{1}{2} m_p (v_0^2 - v_r^2), \tag{S9}$$

where $E_p = \frac{1}{2}\zeta \Delta m_t v_{dc}^2 + E_{ec} + E_l$ is the projectile kinetic energy absorbed by the target and $v_r \sim v_{dc}$ is the projectile's residual velocity. The projectile is arrested when $E_p = E_0$; the impact velocity at this $E_0$ value defines the ballistic limit velocity (commonly denoted $v_{50}$).

For ballistic performance studies, the projectile often stays intact and, if perforation occurs, exits the target with velocity $v_r$. In such cases, target performance evaluation often focuses on ratios like $v_r/v_0 \sim v_{dc}/v_0$ or a normalized variation of Eq. (S9) (see, *e.g.*, [11]). This approach is valid since often $\Delta m_t \ll m_p$ and the projectile remains largely intact. However, when comparing the *HVI performance* of different target materials, using $v_{dc}/v_0$ or Eq. (S9) alone is inadequate because ($i$) the projectile rarely stays intact

for $v_0 > 2.0$ km/s and (*ii*) a large portion of the target mass is often launched uprange/downrange with significant momentum and kinetic energy. For these reasons, incorporating target mass loss ($\Delta m_t$) into a comparative metric is advantageous. One simple approach is based on the maximum theoretical kinetic energy of the debris cloud. In Eq. (S7), the physical conditions $E_{ec} \geq 0$ and $E_l \geq 0$ indicate that

$$\frac{E_{dc}}{E_0} = \left(\alpha + \zeta \frac{\Delta m_t}{m_p}\right) \frac{v_{dc}^2}{v_0^2} \leq \left(1 + \frac{\Delta m_t}{m_p}\right) \frac{v_{dc}^2}{v_0^2} \leq 1, \tag{S10}$$

and

$$\frac{E_{ec} + E_l}{E_0} \leq 1 - \frac{E_{dc}}{E_0} = 1 - \left(\alpha + \zeta \frac{\Delta m_t}{m_p}\right) \frac{v_{dc}^2}{v_0^2}. \tag{S11}$$

In general,

$$\alpha = f\left(\frac{\rho_t}{\rho_p}, \frac{h_t}{d_p}, \frac{T_m}{T_{p,m}}, \frac{\sigma_{t,Y}}{\sigma_{p,Y}}, \frac{E_t}{E_p}, \frac{K_t}{K_p}, \frac{v_0}{\sqrt{\sigma_{t,Y}/\rho_p}}, \frac{\sigma_{t,s}}{\sigma_{t,Y}}, \ldots\right), \tag{S12a}$$

$$\zeta = g\left(\frac{\rho_t}{\rho_p}, \frac{h_t}{d_p}, \frac{T_m}{T_{p,m}}, \frac{\sigma_{t,Y}}{\sigma_{p,Y}}, \frac{E_t}{E_p}, \frac{K_t}{K_p}, \frac{v_0}{\sqrt{\sigma_{t,Y}/\rho_p}}, \frac{\sigma_{t,s}}{\sigma_{t,Y}}, \ldots\right), \tag{S12b}$$

where $T_{p,m}$ denotes the projectile melt temperature, $\sigma_{t,Y}$ and $\sigma_{p,Y}$ the dynamic yield stresses of target and projectile, $E_t$ and $E_p$ their dynamic elastic moduli, and $K_t$ and $K_p$ their dynamic bulk moduli, respectively. The term $\rho_p v_0^2/\sigma_{t,Y}$ represents the damage number, a ratio of inertia to strength, and $\sigma_{t,s}$ indicates the

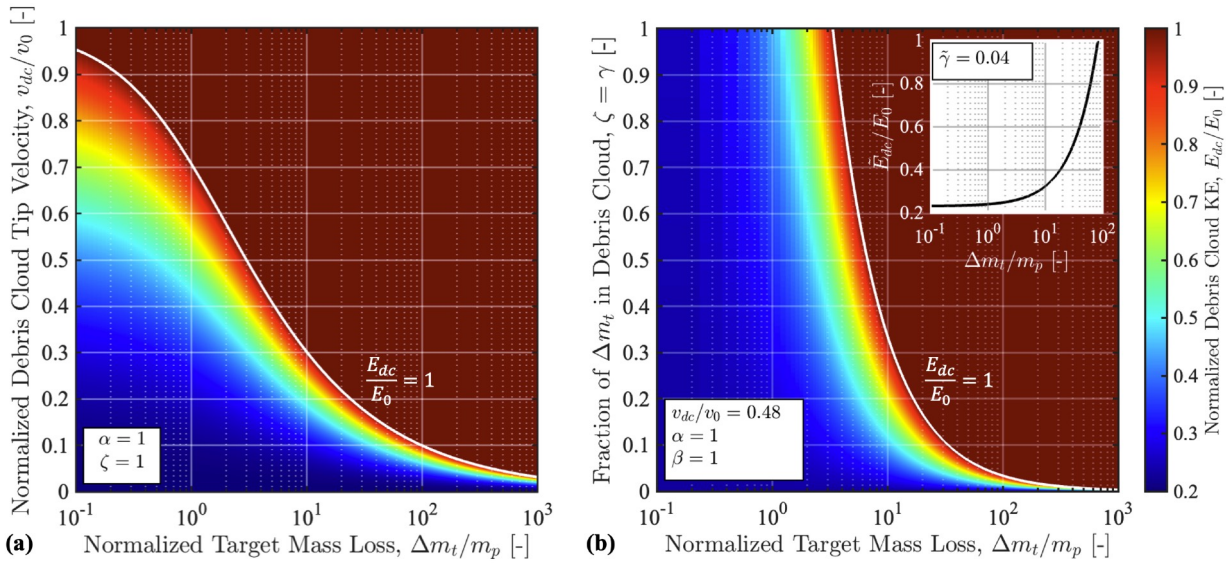


Figure S3: Normalized debris cloud kinetic energy (KE) for varying parameters: (a) debris cloud tip velocity, $v_{dc}/v_0$, versus normalized target mass loss, $\Delta m_t/m_p$; (b) fraction of target mass loss in debris cloud, $\zeta = \gamma$, against $\Delta m_t/m_p$. In both plots, the projectile or its fragments proceed downrange at velocity $v_{dc}$ ($\alpha = 1$). An increase in $\Delta m_t/m_p$ necessitates a reduction in both $v_{dc}/v_0$ and $\zeta$ to preserve a specified debris cloud lethality level. The inset in (b) shows that with $\zeta = \tilde{\gamma} = 0.04$ held constant, a rise in $\Delta m_t/m_p$ leads to an increase in normalized critical debris cloud KE ($\tilde{E}_{dc}/E_0$), ranging from a minimum $(v_{dc}/v_0)^2$ to a maximum of unity.

target's dynamic spall strength [12].

Ideally, $\alpha$ and $\gamma$ should be experimentally determined for specific impact scenarios. Studies using flash X-ray radiography on HVIs of spheres into plates have revealed that, for various $h_t/d_p$ ratios, the projectile or a dense grouping of its fragments lead the debris cloud [13]. This debris cloud "front element" travels at roughly $v_{dc}$, suggesting $\alpha \approx 1$. This estimate is conservative, given that projectile fragments are often denser than those of the target, rendering the front element a significant ballistic threat to structures that follow. Determining $\zeta$ experimentally is challenging due to the often wide distribution of target fragment mass and velocity, with some moving too slowly ($<0.1v_0$) to even contribute to the primary debris cloud formation. Moreover, the largest target fragment can exceed the smallest in size (and mass) by over $10^4$ times, complicating the use of a single high-rate diagnostic tool for comprehensive fragment resolution. In the absence of precise experimental data, $\zeta$ can be estimated using calibrated numerical models/simulations.

For comparing the relative HVI performance of two or more materials with similar densities and identical geometries, precise values of $\alpha$ and $\zeta$ may not be essential given certain assumptions. For example, the clustering of projectile fragments in the debris cloud implies $\alpha \approx 1$. In addition, a conservative supposition can be made that all target fragments in the debris cloud move downrange at velocity $v_{dc}$ ($\beta \approx 1$). Implicit in this assumption is that the ratio of target material in the ejecta cloud to that in the debris cloud is constant for all impact conditions considered. Finally, the ratio $v_{dc}/v_0$ between the two materials is assumed similar and to not significantly vary with $v_0$, a claim supported by studies showing stability in this ratio when $h_t/d_p$ is fixed [5]. In the present study, the average value of $v_{dc}/v_0$ was $\sim$0.45, reaching a maximum of 0.48. For illustration, the ratio $v_{dc}/v_0 = 0.48$ can be held constant for a specific projectile mass, requiring the fraction of $\Delta m_t$ in the debris cloud ($\zeta = \gamma$) to decrease as $\Delta m_t$ increases to sustain a certain lethality level (Fig. S3b). Under these assumptions, a value $\zeta = \tilde{\gamma}$ can be selected to represent the worst-case scenario for a set of $M$ HVI experiments: the target experiencing maximum mass loss where all projectile kinetic energy is transferred to the debris cloud ($E_{dc}/E_0 = 1$):

$$\zeta = \tilde{\gamma} = \min_{1 \le j \le M} \left[ \left( \frac{(v_0^j)^2}{(v_{dc}^j)^2} - 1 \right) \frac{m_p}{\Delta m_t^j} \right], \tag{S13}$$

where $j$ indexes the experimental observations in set $M$ and $m_p$ is assumed to be fixed. The highest HVI-induced normalized target mass loss was $\Delta m_t/m_p \approx 90$, yielding $\tilde{\gamma} \approx 0.04$. This indicates that for the target experiencing the maximum mass loss, if all $E_0$ were transformed into $E_{dc}$, only $0.04\Delta m_t$ would contribute to the debris cloud's kinetic energy. Consequently, this procedure generates a normalized critical debris cloud kinetic energy metric ($\tilde{E}_{dc}/E_0$, Fig. S3b inset) for HVI performance analysis that considers both target mass

loss and debris cloud tip velocity:

$$0 \leq \frac{(v_{dc}^j)^2}{(v_0^j)^2} \leq \frac{\tilde{E}_{dc}^j}{E_0^j} = \left(\tilde{\gamma}\frac{\Delta m_t^j}{m_p} + 1\right)\frac{(v_{dc}^j)^2}{(v_0^j)^2} \leq 1, \tag{S14}$$

where $E_{dc}^j/E_0^j$ is the normalized critical debris cloud kinetic energy for the $j$-th experiment and $\tilde{\gamma} = 0.04$ for the materials and HVI conditions considered in this study ($v_0$ = 2.5, 6.0 km/s, $h_t/d_p = 2$). Notably, Eq. (S14) offers a stricter assessment of debris cloud lethality compared to Eq. (S8), after adjusting for the maximum observed value, *i.e.*,

$$\frac{\tilde{E}_{dc}^j}{E_0^j} \geq \frac{E_{dc,max}^j/E_0^j}{\max\limits_{1\leq j\leq M}[E_{dc,max}^j/E_0^j]}, \quad \text{for all} \quad j \in 1, 2, \ldots, M, \tag{S15}$$

owing to the physical bounds $0 \leq \tilde{\gamma} \leq 1$, or equivalently, $m_p/(m_p + \max \Delta m_t^j) \leq (v_{dc}^j)^2/(v_0^j)^2 \leq 1$ (assuming $m_p$ is fixed and $v_{dc}/v_0$ is roughly constant).[17] As an aside, this procedure (Algorithm 1) was used on previous UHMWPE and HDPE HVI data (see Table S2 and Fig. S4) [5], indicating that HDPE marginally outperformed UHMWPE at various impact velocities, with test temperature and projectile/target geometry held constant.

**Algorithm 1** HVI Performance Comparison of Various Target Materials

1: Identify target materials for HVI performance analysis. Targets must have similar geometries.
2: Prepare and characterize $M$ HVI samples, including mass measurement ($\Delta m_t^j$).
3: Conduct $M$ HVI tests at normal incidence using similar projectiles launched by a suitable launch apparatus, like a 2SLGG.
4: **for** each test $j \in 1, 2, \ldots, M$ **do**
5: Determine projectile impact velocity ($v_0^j$) *via* laser velocimetry, high-speed imaging, *etc.*
6: Capture HVI event with high-speed camera oriented orthogonal to the projectile velocity vector.
7: Calculate debris cloud tip velocity ($v_{dc}^j$) using motion tracking software.
8: **end for**
9: Compute ratios $\Delta m_t^j/m_p$ and $v_{dc}^j/v_0^j$ for each test.
10: Calculate $\tilde{\gamma}$ using Eq. (S13).
11: Use $\tilde{\gamma}$ to compute $\tilde{E}_{dc}^j/E_0^j$, Eq. (S14), for comparison across all tests. A higher $\tilde{E}_{dc}^j/E_0^j$ value implies a potentially more lethal debris cloud.

[17] As $\tilde{\gamma} \longrightarrow 1$, $\frac{\tilde{E}_{dc}^j}{E_0^j} \longrightarrow \frac{E_{dc,max}^j/E_0^j}{\max\limits_{1\leq j\leq M}[E_{dc,max}^j/E_0^j]}$. As $\tilde{\gamma} \longrightarrow 0$, $\frac{\tilde{E}_{dc}^j}{E_0^j} \longrightarrow \frac{(v_{dc}^j)^2}{(v_0^j)^2} \longrightarrow 1$.

*SI.4. Debris Cloud Lethality Comparison for UHMWPE and HDPE Plates with $h_t/d_p = 0.64$*

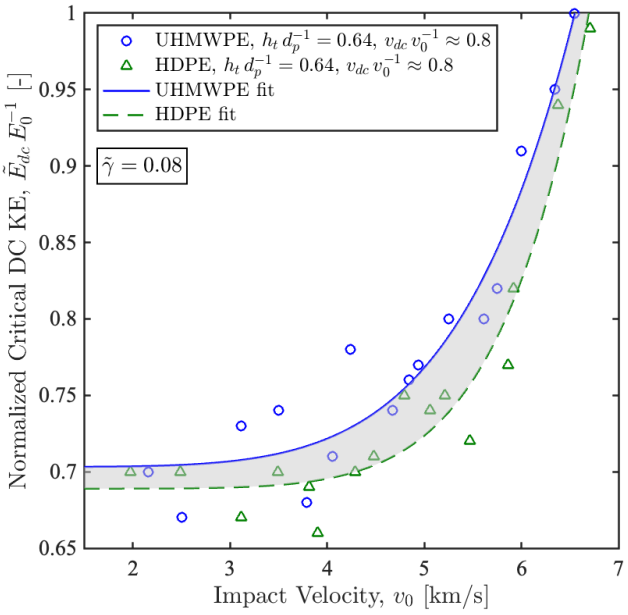


Figure S4: Normalized critical debris cloud KE (lethality) *vs.* impact velocity for data reported by Rogers *et al.* [5]. Power law fits, with R-square values of roughly 0.94, are shown for visualization. Using this comparative metric, HDPE plates marginally outperformed (by ∼5%) UHMWPE plates of similar geometry at room temperature. For all experiments, 10 mm diameter 1050 aluminum spheres ($m_p = 1.41$ g) were launched into 6.35 mm thick targets. Data presented in Table S2.

Table S2: Data from Ref. [5], including $v_0$, $v_{dc}/v_0$, and $\Delta m_t/m_p$ used to compute the $\tilde{E}_{dc}/E_0$ values for UHMWPE and HDPE presented in Fig. S4. For all experiments, 10 mm diameter 1050 aluminum spheres ($m_p = 1.41$ g) were launched into 6.35 mm thick targets.

| No. | Material | $v_0$ (km/s) | $v_{dc}/v_0$ | $\Delta m_t/m_p$ | $\tilde{E}_{dc}/E_0$ |
|---|---|---|---|---|---|
| 1 | UHMWPE | 2.16 | 0.80 | 1.07 | 0.70 |
| 2 | UHMWPE | 2.50 | 0.79 | 1.05 | 0.67 |
| 3 | UHMWPE | 3.11 | 0.81 | 1.28 | 0.73 |
| 4 | UHMWPE | 3.50 | 0.81 | 1.64 | 0.74 |
| 5 | UHMWPE | 3.79 | 0.77 | 1.79 | 0.68 |
| 6 | UHMWPE | 4.05 | 0.79 | 1.95 | 0.71 |
| 7 | UHMWPE | 4.24 | 0.82 | 1.97 | 0.78 |
| 8 | UHMWPE | 4.67 | 0.79 | 2.17 | 0.74 |
| 9 | UHMWPE | 4.84 | 0.80 | 2.28 | 0.76 |
| 10 | UHMWPE | 4.94 | 0.80 | 2.45 | 0.77 |
| 11 | UHMWPE | 5.25 | 0.82 | 2.48 | 0.80 |
| 12 | UHMWPE | 5.61 | 0.81 | 2.66 | 0.80 |
| 13 | UHMWPE | 5.75 | 0.82 | 2.61 | 0.82 |
| 14 | UHMWPE | 6.00 | 0.87 | 2.63 | 0.91 |
| 15 | UHMWPE | 6.34 | 0.88 | 2.72 | 0.95 |
| 16 | UHMWPE | 6.54 | 0.90 | 2.80 | 1.00 |
| 17 | HDPE | 1.97 | 0.81 | 0.66 | 0.70 |
| 18 | HDPE | 2.49 | 0.81 | 0.76 | 0.70 |
| 19 | HDPE | 3.11 | 0.79 | 1.00 | 0.67 |
| 20 | HDPE | 3.49 | 0.80 | 1.10 | 0.70 |
| 21 | HDPE | 3.81 | 0.79 | 1.19 | 0.69 |
| 22 | HDPE | 3.90 | 0.77 | 1.26 | 0.66 |
| 23 | HDPE | 4.29 | 0.80 | 1.41 | 0.70 |
| 24 | HDPE | 4.48 | 0.79 | 1.51 | 0.71 |
| 25 | HDPE | 4.79 | 0.82 | 1.55 | 0.75 |
| 26 | HDPE | 5.06 | 0.80 | 1.73 | 0.74 |
| 27 | HDPE | 5.21 | 0.81 | 1.85 | 0.75 |
| 28 | HDPE | 5.47 | 0.79 | 2.00 | 0.72 |
| 29 | HDPE | 5.86 | 0.81 | 2.03 | 0.77 |
| 30 | HDPE | 5.92 | 0.84 | 1.91 | 0.82 |
| 31 | HDPE | 6.37 | 0.90 | 2.20 | 0.94 |
| 32 | HDPE | 6.70 | 0.92 | 2.17 | 0.99 |

*SI.5. Additional High-Speed Images of HVIs Showing Debris Cloud Development*

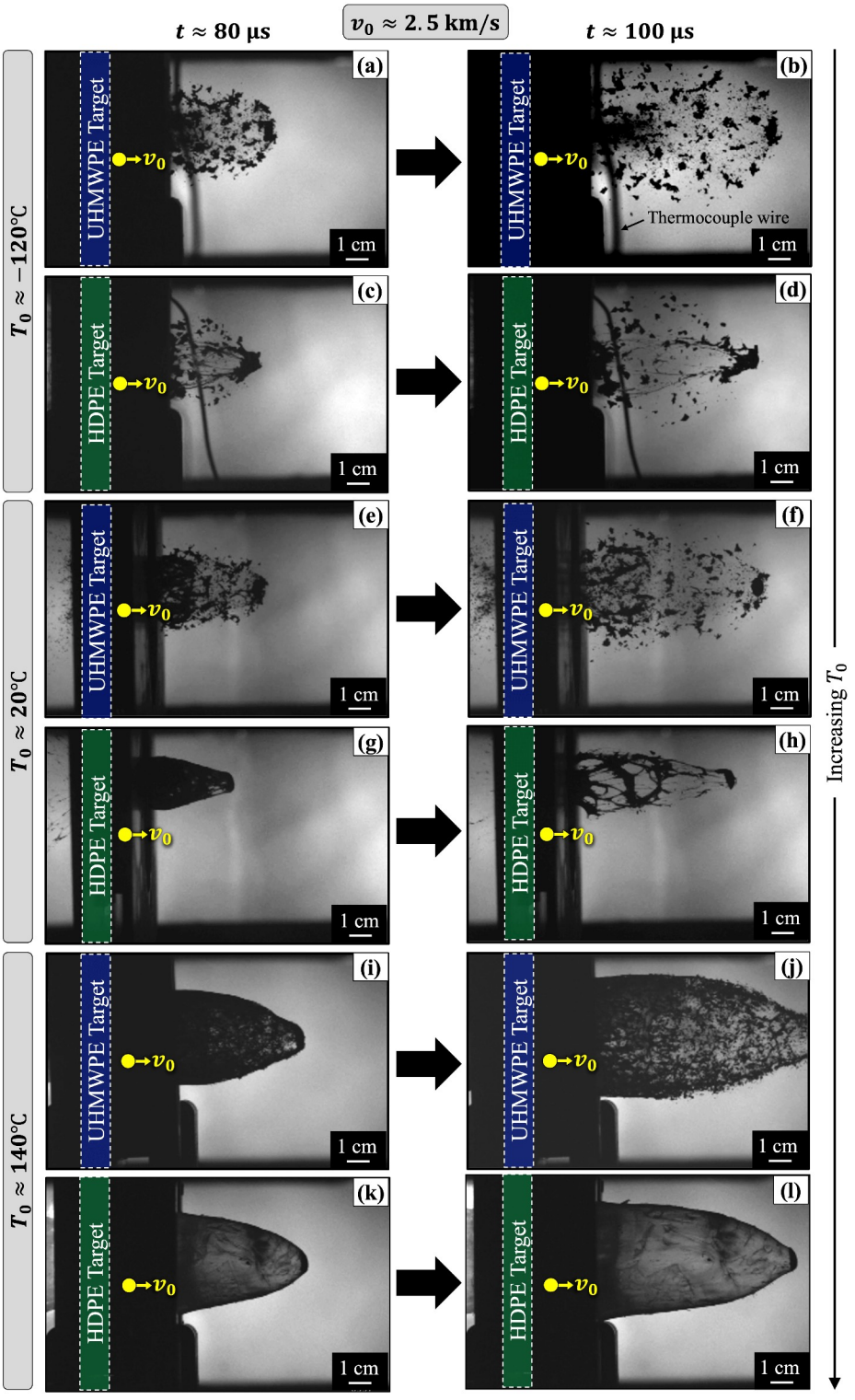


Figure S5: Debris clouds from HVIs of $d_p = 6.35$ mm aluminum spheres into 12.7 mm thick UHMWPE and HDPE plates at $v_0 \approx 2.5$ km/s, captured at two time instances ($t \approx 80$ µs and 100 µs; columns, in ascending order) and at three initial target temperatures (rows, in ascending order): (a–d) $T_0 \approx -120$°C, (e–h) $T_0 \approx 20$°C, and (i–l) $T_0 \approx 140$°C.

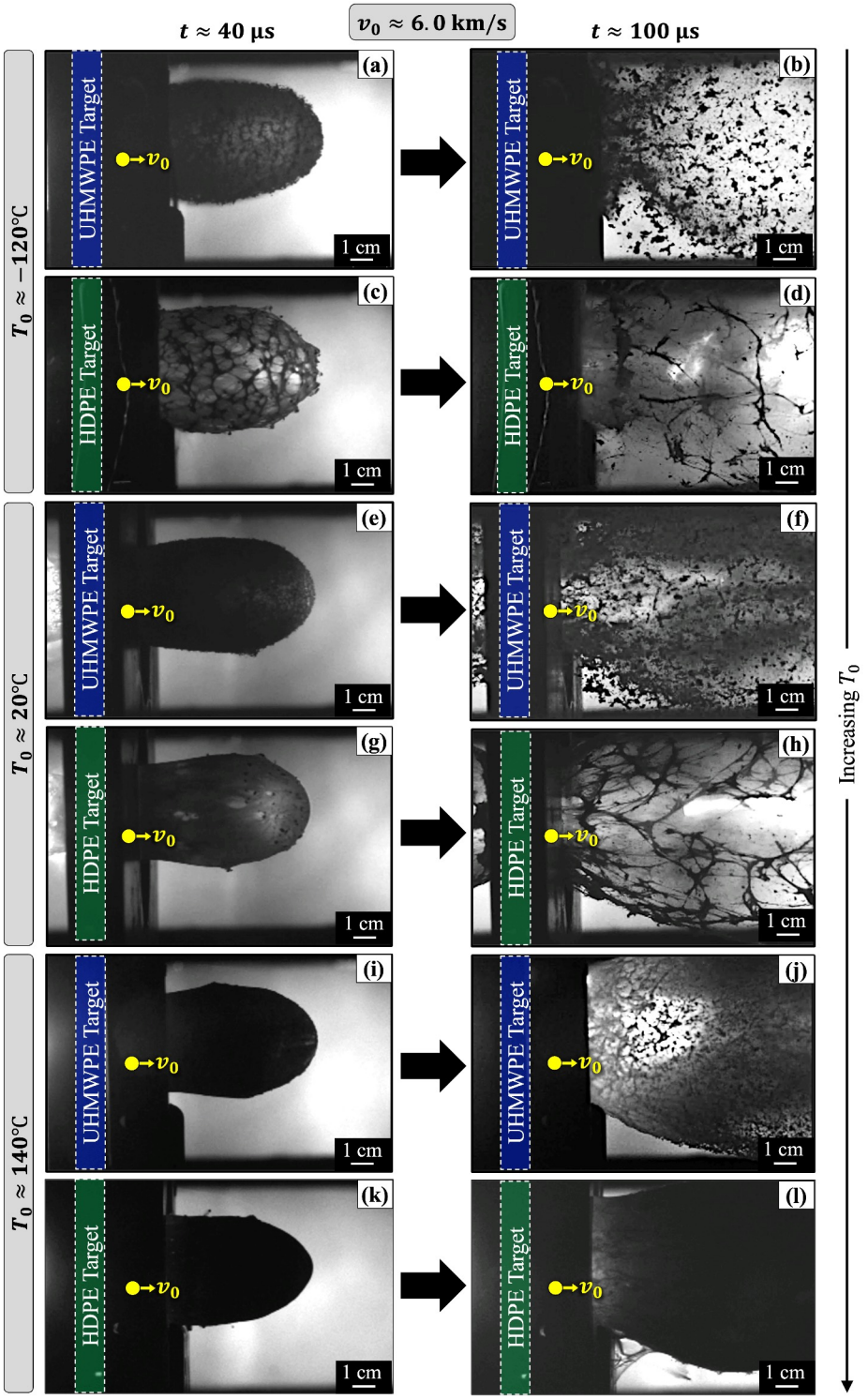


Figure S6: Debris clouds from HVIs of $d_p = 6.35$ mm aluminum spheres into 12.7 mm thick UHMWPE and HDPE plates at $v_0 \approx 6.0$ km/s, captured at two time instances ($t \approx 40$ µs and 100 µs; columns, in ascending order) and at three initial target temperatures (rows, in ascending order): (a–d) $T_0 \approx -120$°C, (e–h) $T_0 \approx 20$°C, and (i–l) $T_0 \approx 140$°C.

*SI.6. Results of HVI Numerical Simulations*

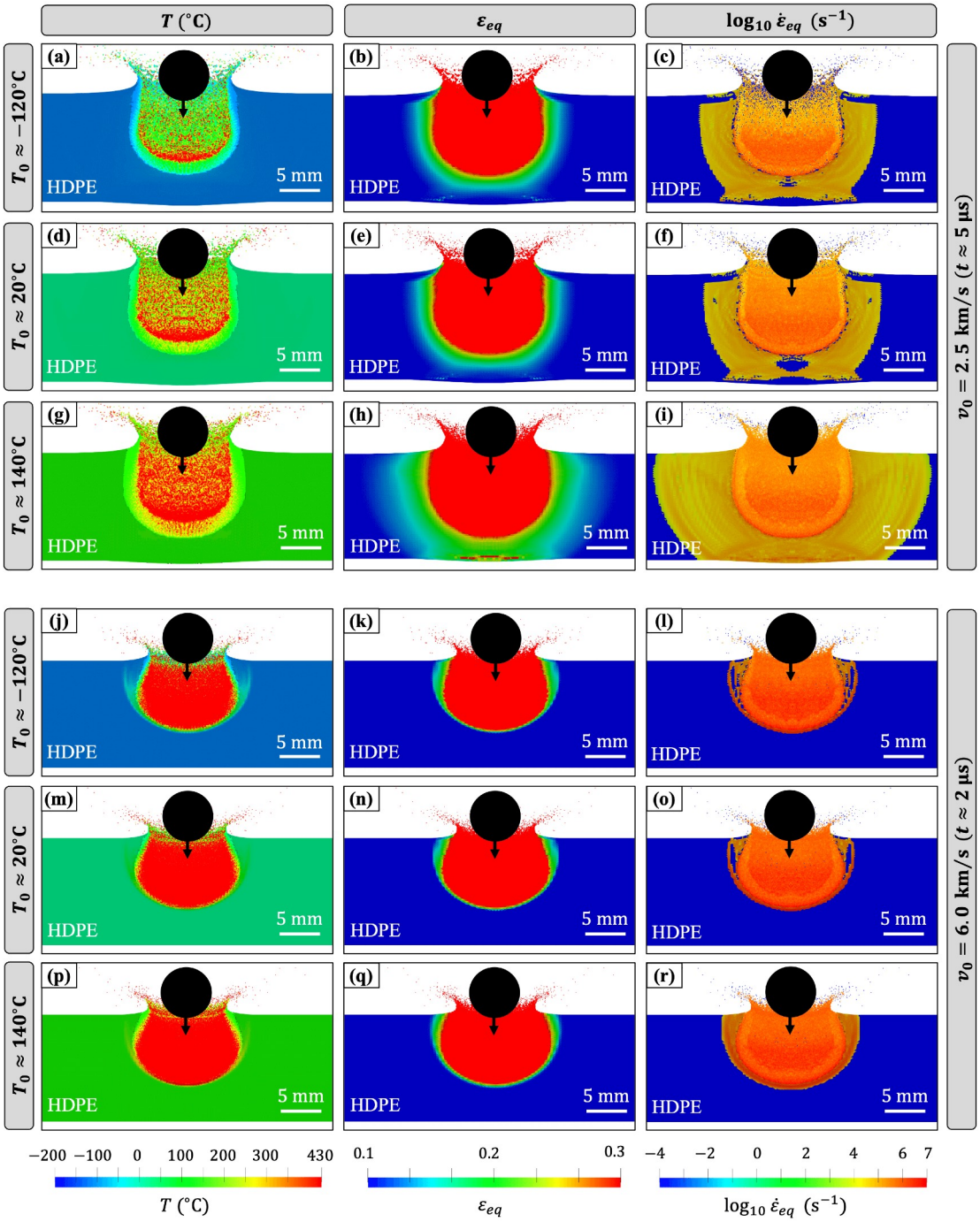


Figure S7: Simulation snapshots of temperature $T$, equivalent plastic strain $\varepsilon_{eq}$, and equivalent plastic strain rate ($\dot{\varepsilon}_{eq}$) for $d_p = 6.35$ mm aluminum sphere HVIs into 12.7 mm thick representative HDPE plates at (a–i) $v_0 \approx 2.5$ km/s and (j–r) $v_0 \approx 6.0$ km/s. Snapshots are shown at times corresponding to when the target is halfway perforated. Simulated projectiles were hidden from the snapshots to better showcase the targets' conditions. A scaled projectile *icon* is superimposed on each image for reference. For each $v_0$, the snapshot time reflects the moment the target is approximately halfway perforated. Target temperatures reach the thermal degradation temperature of HDPE ($T \approx 430$°C), and strain rates reach $\dot{\varepsilon}_{eq} = 10^7$ s$^{-1}$. Material models and parameters were sourced from Ref. [14].

*SI.7. Additional Target Images*

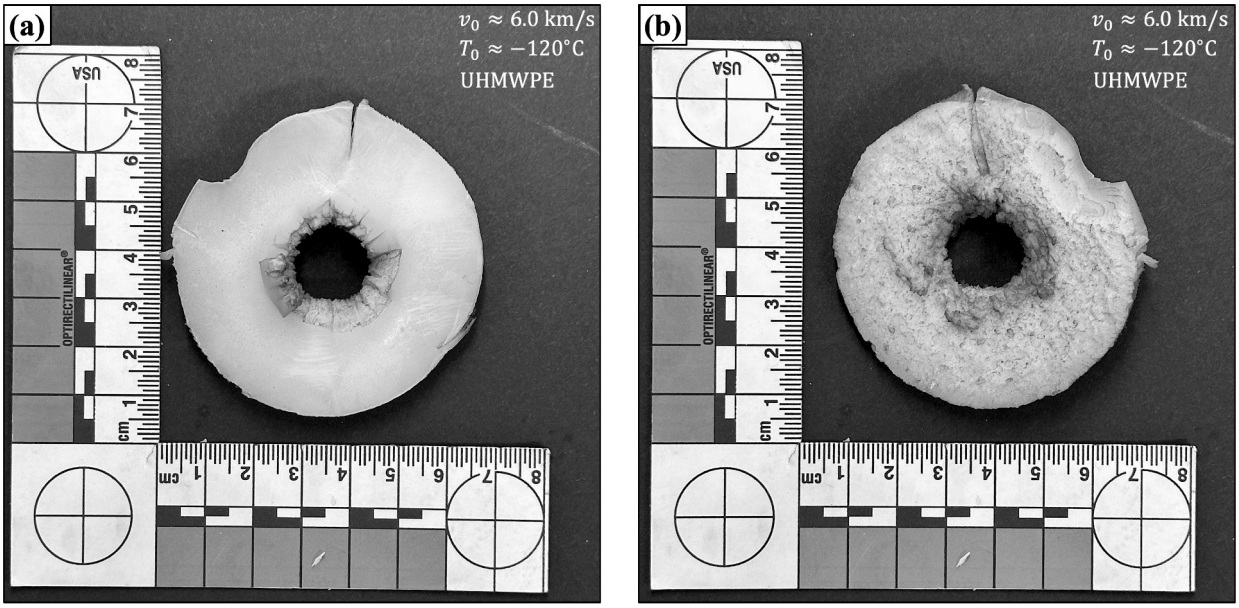


Figure S8: Front (left) and back side (right) images of the target spall fragment due to cone fracture of the -120°C UHMWPE target impacted at 6.0 km/s (*cf.* Fig. 8d).

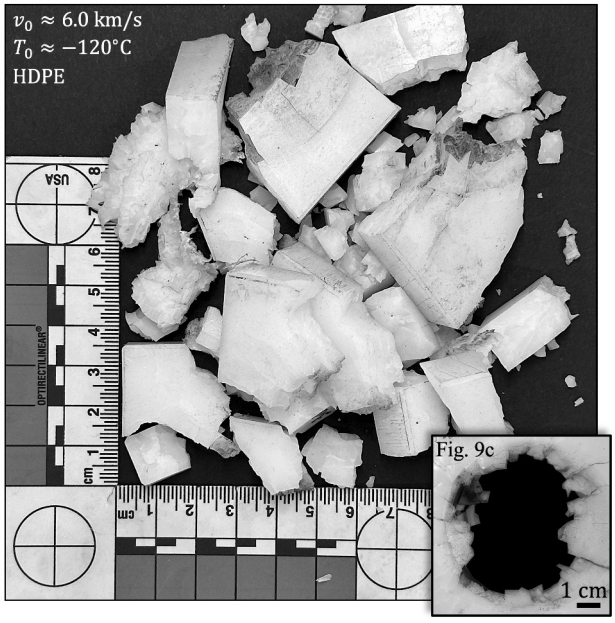


Figure S9: Fragments of the -120°C HDPE plate impacted at $v_0 \approx 6.0$ km/s. An image displaying the perforation was captured before the target was removed from the fixture (see inset and Fig. 9d).

*SI.8. The Transition Velocity Regime for UHMWPE and HDPE*

For a specific projectile-target material pair, discerning the transition from high-velocity impact conditions (where material response is dominated by strength) to hypervelocity impact phenomena (characterized by hydrodynamic behavior) is crucial for understanding the materials' states, as well as their primary deformation and failure mechanisms. A straightforward method for defining this transition regime entails identifying the impact velocities that result in material shocks strong enough to trigger incipient and complete melting of the projectile/target [15].[18] These critical velocities can be approximated using the one-dimensional (1D) Rankine-Hugoniot equations, which, for a coordinate system moving with the shock front traveling through a medium, can be expressed as

$$\frac{u}{U} = \left(1 - \frac{\rho_0}{\rho}\right) \qquad \textit{mass conservation}, \tag{S16}$$

$$p - p_0 = \rho_0 U u \qquad \textit{momentum conservation}, \tag{S17}$$

$$e - e_0 = \frac{1}{2}(p + p_0)\left(1 - \frac{\rho_0}{\rho}\right) = \frac{1}{2}\rho_0 u^2 \qquad \textit{energy conservation}, \tag{S18}$$

where $u$ represents the material particle velocity; $U$ the shock front velocity; $\rho_0$ and $\rho$ the densities before and after the shock, respectively; $p_0$ and $p$ the momenta before and after the shock, respectively; and $e_0$ and $e$ the internal energies before and after the shock, respectively. Equations (S17)–(S18), combined with the kinematic condition $v_0 = u_p + u_t$, can be used to partition the specific internal energy of the projectile and target upon impact:

$$e_p = \left(\frac{u_p/u_t}{1 + u_p/u_t}\right)^2 k_0, \tag{S19}$$

and

$$e_t = \frac{u_p/u_t}{(1 + u_p/u_t)^2} k_0, \tag{S20}$$

where subscripts $p$ and $t$ denote the projectile and target materials, respectfully, and $k_0 = \frac{1}{2}\rho_{0,p} v_0^2$. An equation of state (EOS) is also required. For simplicity, a simple EOS was used in this work, *i.e.*,

$$U_{(p/t)} = s_{(p/t)} u_{(p/t)} + a_{(p/t)} \tag{S21}$$

where $s$ is an empirical fitting parameter and $a = \sqrt{K/\rho_0}$ is the material sound velocity at zero pressure ($K$ is the material bulk modulus). Equations (S19)–(S21) can be used to calculate the "trapped" residual

[18] The following transition regime derivation/definition was first reported by Signetti *et al.* [15].

internal energy in the projectile/target that can contribute to heating:

$$e_{h,(p/t)} = e_{(p/t)} - \frac{1}{\rho_{(p/t)}} \int_{\rho_{0,(p/t)}}^{\rho_{(p/t)}} r \, d\rho \Bigg|_{S=\text{const.}}, \tag{S22}$$

where the second term represents the reversible energy from isentropic ($S = \text{const}$) expansion due to pressure release (*i.e.*, rarefaction wave). Incipient melting for each material occurs when the internal energy within it equals

$$e_{m,(p/t)} = \rho_{0,(p/t)} \int_{T_0}^{T_{m,(p/t)}} c_{v,(p/t)}(T) \, dT, \tag{S23}$$

where $T_m$ is the melting temperature of the material, $c_v(T)$ is its specific heat capacity at constant volume, and $T$ is the variable temperature. Complete melting of the material occurs when

$$e_{h,(p/t)}(v_0) = e_{m,(p/t)} + e_{fus,(p/t)}, \tag{S24}$$

where $e_{fus,(p/t)}$ is the enthalpy of fusion. Thus, for a given projectile-target material combination, the transition velocity regime can be defined as

$$\min\left(v_{m,p}, v_{m,t}\right) < v_0 < \max\left(v_{fus,p}, v_{fus,t}\right), \tag{S25}$$

where $v_{m,(p/t)}$ and $v_{fus,(p/t)}$ are the impact velocities leading to incipient and complete melting, respectively, of the projectile/target material.

This method was applied here to estimate the transition regime for the aluminum projectiles impacting the PE targets. Given their similar thermal properties and densities, both PEs were characterized succinctly in one calculation using representative values for $T_m$, $\rho_0$, $c_v$, $e_{fus}$, $a$, and $s$. The parameter values used for the projectile/target are summarized in Table S3. Figure S10 displays the residual specific internal energy in the projectile/target as a function of impact velocity. The target undergoes a transition to predominantly hydrodynamic behavior at a relatively low velocity ($v_0 \sim 2.5$ km/s) compared to the aluminum sphere ($v_0 \sim 9.0$ km/s). Hence, the complete transition velocity regime is $2.0 < v_0 < 9.1$ km/s.

Table S3: Material data for transition velocity regime calculations sourced from Refs. [16, 17].

| No. | Parameter | Projectile (Al) | Target (PE) | Units |
|---|---|---|---|---|
| 1 | $T_m$ | 650 | 130 | °C |
| 2 | $\rho_0$ | 2.70 | 0.95 | g/cm$^3$ |
| 3 | $c_v$ | 0.90 | 2.00 | J/(g·°C) |
| 4 | $e_{fus}$ | 1.06 | 0.20 | J/mm$^3$ |
| 5 | $a$ | 5.25 | 2.88 | km/s |
| 6 | $s$ | 1.37 | 1.68 | ··· |

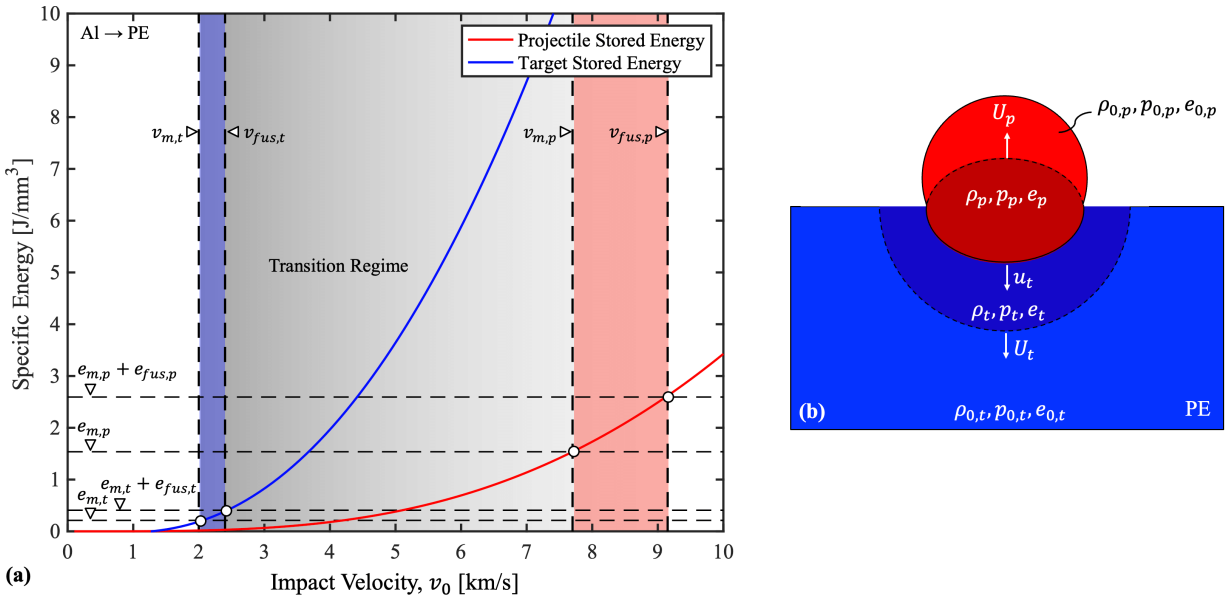


Figure S10: Transition velocity regime (high-velocity to hypervelocity) for an aluminum sphere impacting a HDPE plate, marked by the onset and complete melting of materials [18]. This regime is defined for the sphere with initial density $\rho_{p,0}$, momentum $p_{p,0}$, and internal energy $e_{p,0}$, and for the HDPE plate with initial density $\rho_{t,0}$, momentum $p_{t,0}$, and internal energy $e_{t,0}$. The transition velocity region ranges from $v_{m,t} = 2.0$ km/s to $v_{fus,p} = 9.1$ km/s for both the projectile and target, and $v_{m,t} = 2.0$ km/s to $v_{fus,t} = 2.3$ km/s for the target alone. These calculations indicate PE targets melt and exhibit hydrodynamic behavior at velocities $v_0 \geq 2.5$ km/s.

## References for Supplementary Material


[1] R. C. Huber *et al.*, "In situ x-ray diffraction of high density polyethylene during dynamic drive: Polymer chain compression and decomposition," *Journal of Applied Physics*, vol. 130, no. 17, 2021.

[2] C. Xie, "Interactive heat transfer simulations for everyone," *The Physics Teacher*, vol. 50, no. 4, pp. 237–240, 2012.

[3] W. P. Schonberg *et al.*, "Hypervelocity impact physics," NASA, Tech. Rep., 1991.

[4] W. Herrmann and J. S. Wilbeck, "Review of hypervelocity penetration theories," *International Journal of Impact Engineering*, vol. 5, no. 1-4, pp. 307–322, 1987.

[5] J. A. Rogers *et al.*, "Hypervelocity impact response of monolithic UHMWPE and HDPE plates," *International Journal of Impact Engineering*, vol. 161, p. 104 081, 2022.

[6] J.-H. Cha *et al.*, "Ultra-high-molecular-weight polyethylene as a hypervelocity impact shielding material for space structures," *Acta Astronautica*, vol. 168, pp. 182–190, 2020.

[7] K. Callahan *et al.*, "High strain rate failure behavior of polycarbonate plates due to hypervelocity impact," *Macromolecules*, vol. 55, no. 21, pp. 9640–9649, 2022.

[8] S. Khatiwada *et al.*, "Hypervelocity impact experiments on epoxy/ultra-high molecular weight polyethylene fiber composites reinforced with single-walled carbon nanotubes," *Procedia Engineering*, vol. 58, pp. 4–10, 2013.

[9] K. Qu *et al.*, "Ballistic performance of multi-layered aluminium and uhmwpe fibre laminate targets subjected to hypervelocity impact by tungsten alloy ball," *Composite Structures*, vol. 253, p. 112 785, 2020.

[10] E. Christiansen *et al.*, "Enhanced meteoroid and orbital debris shielding," *International Journal of Impact Engineering*, vol. 17, no. 1-3, pp. 217–228, 1995.

[11] S. Morye *et al.*, "Modelling of the energy absorption by polymer composites upon ballistic impact," *Composites science and technology*, vol. 60, no. 14, pp. 2631–2642, 2000.

[12] Q.-M. Tan, *Dimensional analysis: with case studies in mechanics*. Springer Science & Business Media, 2011.

[13] A. J. Piekutowski, "Characteristics of debris clouds produced by hypervelocity impact of aluminum spheres with thin aluminum plates," *International Journal of Impact Engineering*, vol. 14, no. 1-4, pp. 573–586, 1993.

[14] J. Rogers *et al.*, "Simulating hypervelocity impacts to high-density polyethylene," in *AIAA SCITECH 2023 Forum*, 2023, p. 2021.

[15] S. Signetti and A. Heine, "Characterization of the transition regime between high-velocity and hypervelocity impact: Thermal effects and energy partitioning in metals," *International Journal of Impact Engineering*, vol. 151, p. 103 774, 2021.

[16] R. F. Prater *et al.*, "Hypervelocity impact: Material strength effects on crater formation and shock propagation in three aluminum alloys," Ph.D. dissertation, Air Force Institute of Technology., 1970.

[17] F. Dowell, "Simple eos for linear (high-density) polyethylene (marlex)," Los Alamos National Lab.(LANL), Los Alamos, NM (United States), Tech. Rep., 1982.

[18] S. Signetti and A. Heine, "Transition regime between high-velocity and hypervelocity impact in metals–a review of the relevant phenomena for material modeling in ballistic impact studies," *International Journal of Impact Engineering*, vol. 167, p. 104 213, 2022.